

# PANDROMEDA - FIRST RESULTS FROM THE HIGH-CADENCE MONITORING OF M31 WITH PAN-STARRS 1

C.-H. Lee<sup>1,2,3</sup>, A. Riffeser<sup>1,2</sup>, J. Koppenhoefer<sup>2,1</sup>, S. Seitz<sup>1,2</sup>, R. Bender<sup>1,2</sup>, U. Hopp<sup>1,2</sup>, C. Gössl<sup>1,2</sup>, R. P. Saglia<sup>2,1</sup>, J. Snigula<sup>2,1</sup>, W. E. Sweeney<sup>4</sup>, W. S. Burgett<sup>4</sup>, K. C. Chambers<sup>4</sup>, T. Grav<sup>5</sup>, J. N. Heasley<sup>4</sup>, K. W. Hodapp<sup>4</sup>, N. Kaiser<sup>4</sup>, E. A. Magnier<sup>4</sup>, J. S. Morgan<sup>4</sup>, P. A. Price<sup>6</sup>, C. W. Stubbs<sup>7</sup>, J. L. Tonry<sup>4</sup>, R. J. Wainscoat<sup>4</sup>.

## ABSTRACT

The Pan-STARRS 1 (PS1) survey of M31 (PAndromeda) is designed to identify gravitational microlensing events, caused by bulge and disk stars (self-lensing) and by compact matter in the halos of M31 and the Milky Way (halo lensing, or lensing by MACHOs). With the 7 deg<sup>2</sup> FOV of PS1, the entire disk of M31 can be imaged with one single pointing. Our aim is to monitor M31 with this wide FOV with daily sampling (20 mins/day). In the 2010 season we acquired in total 91 nights toward M31, with 90 nights in the  $r_{P1}$  and 66 nights in the  $i_{P1}$ . The total integration time in  $r_{P1}$  and  $i_{P1}$  are 70740s and 36180s, respectively. As a preliminary analysis, we study a  $40' \times 40'$  sub-field in the central region of M31, a  $20' \times 20'$  sub-field in the disk of M31 and a  $20' \times 20'$  sub-field for the investigation of astrometric precision. We demonstrate that the PSF is good enough to detect microlensing events. We present light curves for 6 candidate microlensing events. This is a competitive rate compared to previous M31 microlensing surveys. We finally also present one example light curve for Cepheids, novae and eclipsing binaries in these sub-fields.

*Subject headings:* microlensing – M31 – variable stars

---

<sup>1</sup>University Observatory Munich, Scheinerstrasse 1, 81679 Munich, Germany

<sup>2</sup>Max Planck Institute for Extraterrestrial Physics, Giessenbachstrasse, 85748 Garching, Germany

<sup>3</sup>Graduate Institute of Astronomy, National Central University, Jhongli 32001, Taiwan

<sup>4</sup>Institute for Astronomy, University of Hawaii at Manoa, Honolulu, HI 96822, USA

<sup>5</sup>Planetary Science Institute, 1700 East Fort Lowell, Suite 106, Tucson, AZ 85719, USA

<sup>6</sup>Department of Astrophysical Sciences, Princeton University, Princeton, NJ 08544, USA

<sup>7</sup>Department of Physics, Harvard University, Cambridge, MA 02138, USA

## 1. Introduction

Since the seminal paper by Paczynski (1986), microlensing has been used as an elegant way to probe the massive compact halo object (MACHO) content in our Milky Way. Various experiments have been conducted (e.g. MACHO, EROS, OGLE, MOA) targeting the Magellanic Clouds to constrain the MACHO mass fraction in the Milky Way halo. However, the results remain uncertain because of the self-lensing contamination (Sahu 1994; Alcock *et al.* 2000; Tisserand *et al.* 2007; Wyrzykowski *et al.* 2009, 2010, 2011a,b; Calchi Novati & Mancini 2011).

On the other hand, Crotts (1992) proposed to target M31 to search for MACHOs as dark matter candidates in spiral galaxies. This is because we can have multiple lines of sight toward M31 to better discriminate self-lensing from halo lensing. For example, the far-side of M31 experiences a higher column density of MACHOs than the near-side, thus a spatial asymmetry of the lensing events should show up if a significant MACHO component exists in the halo of M31. A description of the current status of M31 microlensing searches and the theory of microlensing in crowded fields is given in Calchi Novati (2010) and references therein. To summarize this review, previous M31 projects (e.g. POINT-AGAPE (Aurière *et al.* 2001), MEGA (Crotts *et al.* 2001)) have monitored  $\approx 30' \times 30'$  large fields of M31 on the near and far side of the disk while avoiding the central bulge. The WeCAPP (Riffeser *et al.* 2001) team took another approach and monitored a  $17.2' \times 17.2'$  field centered on the M31 center. They have detected  $\sim 10$  events in their 11-year campaign (Riffeser *et al.* in prep.)

The result of the POINT-AGAPE team suggests the existence of MACHOs to explain some of the events (Calchi Novati *et al.* 2005), while the MEGA team claims that the result of their 14 microlensing events (de Jong *et al.* 2006), though 2 of them are more likely to be supernovae (Cseresnjés *et al.* 2005), is reconcilable with self-lensing scenario. Few possible issues on the MEGA results have been addressed by the analysis of Ingrosso *et al.* (2006, 2007). One aspect is that the dust in the M31 disk (Montalto *et al.* 2009) yields an asymmetric detection efficiency of true variables and microlensing events and thus has to be included in a quantitative modeling. The other aspect is that the total number of events found is still not large enough to allow for small errors in statistical analyses on the MACHO fraction of M31. The investigation of the asymmetric signal, the spatial distribution and the total number of events requires large fields to be observed. Another point is the time sampling: Because the full-width-half-maximum (FWHM) timescale of the microlensing events in M31 are estimated to be shorter than a few days (Riffeser *et al.* 2006), one requires a higher time-resolution to detect these events. The POINT-AGAPE and MEGA project have observations every four nights on average (Paulin-Henriksson *et al.* 2003). Riffeser *et al.* (2003)

focused on the  $17.2' \times 17.2'$  FOV in the bulge of M31 with daily observations.

Ongoing campaigns attempt to monitor the inner region of M31 with higher cadence. For example, the ANGSTROM (Andromeda Galaxy Stellar Robotic Microlensing) collaboration employs a world-wide newtork of 2-meter telescopes to allow for 24-hour surveillance of the inner bulge ( $4.6' \times 4.6'$  FOV) of M31 (Kerins *et al.* 2006). The PLAN (Pixel Lensing Andromeda) collaboration aims for consecutive-nights campaigns for two fields (with  $13' \times 12.6'$  FOV each) around the inner region of M31 (Calchi Novati *et al.* 2009), which lead to the first finite-source microlensing event, OAB-N2, toward M31 (Calchi Novati *et al.* 2010). The analysis on this event, as well as the bright event GL1/PA-S3 (Riffeser *et al.* 2008) and PA-N1 (Aurière *et al.* 2001), favors a MACHO senario relative to self-lensing. However, a comprehensive study of the MACHO content in the halo of M31 and constraints on the self-lensing rate requires a large FOV survey with daily sampling. This is only possible with the advent of PAndromeda.

PAndromeda is one of the 12 key projects within the scope of Pan-STARRS 1 (see Kaiser *et al.* 2010; Hodapp *et al.* 2004; Tonry & Onaka 2009, for a detailed description of the PS1 system, optical design and the imager). PAndromeda is designed to identify microlensing events toward M31 with high cadence observations (0.5 h per night for a time span of 5 months per year). With the large FOV of Pan-STARRS 1, it is possible to monitor the entire disk of M31 with one single exposure (see Fig. 1). This enables us to compare the self-lensing event rate (caused by bulge and disk stars within M31) to the prediction from the theoretical calculation (Riffeser *et al.* 2006) with a certain detection efficiency (which is given from the set-up of PAndromeda and simulations). The merit of PAndromeda is the ability to perform a differential measurement across the entire M31 disk. With similar PSF and exact cadence for each image and filter, the detection efficiency mostly varies due to M31 background light. The impacts of PSF variations and cadence are rather small. A discrepancy between the observed and theoretical self-lensing event rate can indicate that the assumptions in the M31 model under consideration (e.g. stellar population) might need to be improved (Saglia *et al.* 2010).

The microlensing event rate will help us to constrain the mass-fraction of compact objects in M31 and the Milky Way halo, as well as the mass function at the low mass end of the M31 bulge. PAndromeda further aims to shed light on the stellar population properties of M31 based on the color profiles, surface-brightness (SFB) fluctuations, resolved stars and variables. It will thus improve our understanding of the mix of stellar ages and metallicities in the halo, bulge, stellar streams and dwarfs of M31. This information is required for an accurate interpretation of the microlensing events. For long timescale events, PAndromeda has the potential to detect sub-stellar objects by means of excursions from the standard

light curve due to companion objects (similar to the candidate discussed by An *et al.* 2004b; Ingrosso *et al.* 2009). In addition to microlensing, the high-cadence of PAndromeda data-set can also shed light on the variables (see e.g. An *et al.* 2004a; Fliri *et al.* 2006) and nova (see e.g. Darnley *et al.* 2004, 2006; Lee *et al.* 2011) in M31.

This paper is organized as follows. In section 2 we present the survey parameters and observations done in 2010. We give a detailed description of our data reduction, data analysis and demonstrate the data quality of the 2010 observation season in section 3. The variables detected in the PAndromeda data-set are presented in section 4. An overview of the microlensing events is shown in section 5, followed by an outlook in section 6. We conclude the paper in section 7.

## 2. PAndromeda Survey Parameters and Observations in 2010

The PAndromeda project is one of the 12 key projects of PS1. It monitors M31, the Andromeda galaxy. The PAndromeda survey is also one of the Pan-STARRS medium deep fields (MDFs) and is called MD0 alternatively. PS1 observations are carried out with the 1.8m Panoramic Survey Telescope and Rapid Response System (Pan-STARRS) located at Haleakala in Hawaii. The camera used is currently the largest one in the world.

It consists of 60 detectors in an  $8 \times 8$  array with empty corners. Each detector is segmented in an  $8 \times 8$  array of  $590 \times 598$  pixel cells with gaps between cells of 19 and 13 pixel widths in the column and row dimensions, respectively. In addition, between each detector there are gaps of approximately 300 pixels in both directions. A single detector therefore consists of a  $4872 \times 4824$  pixel array. Since pixels have a size of  $10 \mu\text{m}$  which corresponds to  $0.258''$  in the focal plane the FOV of each detector is  $20.95' \times 20.74'$  and the total FOV of the 60 detector array is about 7 degrees<sup>2</sup>. The layout of the detector surface is illustrated below in Fig 1.

PAndromeda started the first observation season in 2010 and monitored M31 from 23/07/2010 to 27/12/2010. The M31 observations are done in  $r_{P1}$  and  $i_{P1}$ -band. We use two filters to confirm microlensing events from their achromaticity. We acquired 90 nights in  $r_{P1}$  and 66 nights in  $i_{P1}$ . The total number of images and integration times obtained in the first observing season of PAndromeda are listed in Table 1.

The 0.5 h integration time per night was divided into two observation blocks separated by 3 to 5 hours in order to trace microlensing events with timescales shorter than 1 day. The observation cadence is shown in Fig. 2.

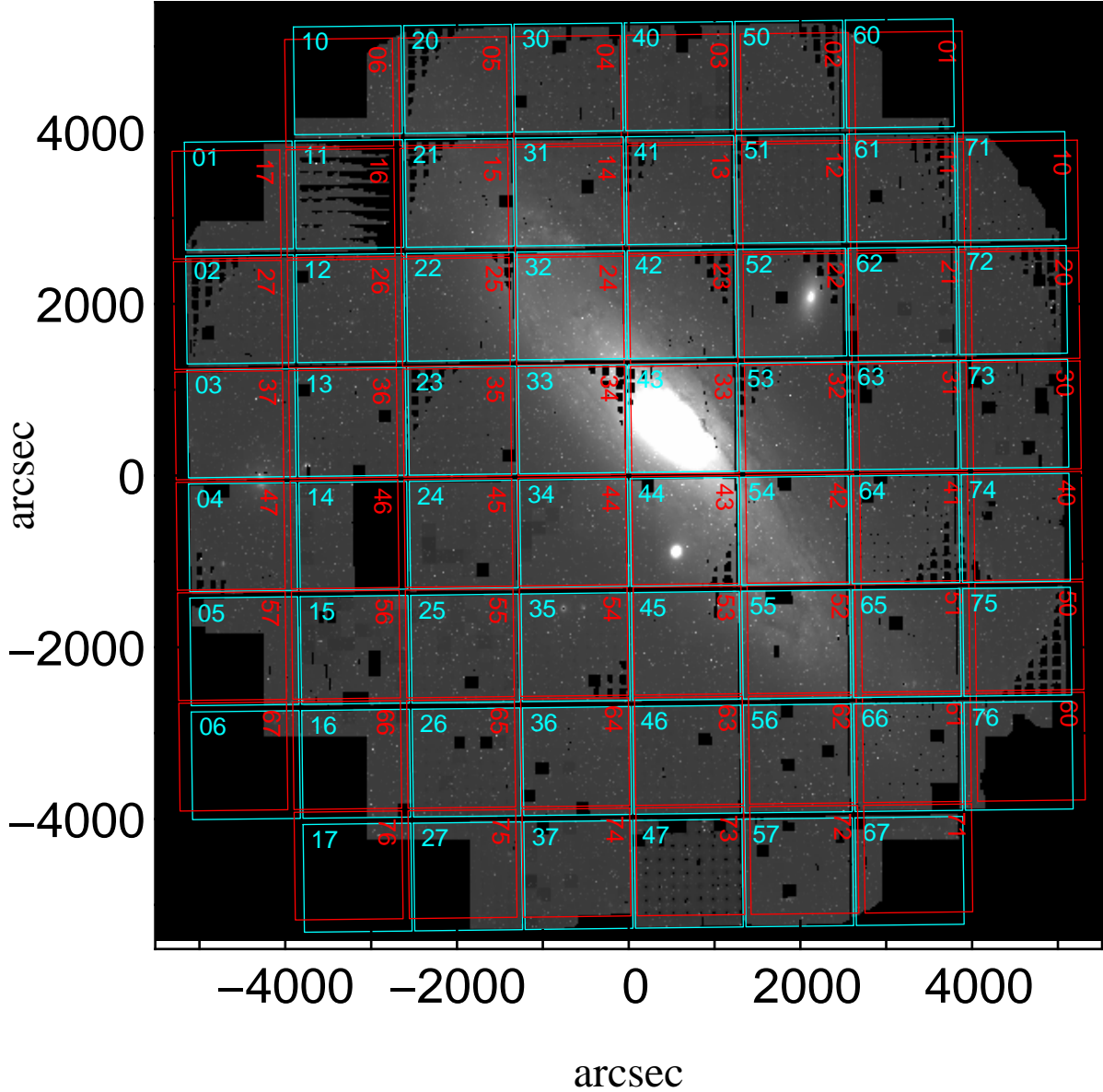


Fig. 1.— The Giga Pixel Camera (GPC) and its 60 detectors labeled by the blue and red grids. The red numbering indicates the same detector corresponding to the blue numbering, but rotated with 90 degrees during the observation. Each detector is composed of  $4872 \times 4824$  pixel with  $0.258''$  per pixel (Tonry & Onaka 2009). The field of view of GPC is  $\sim 7$  degree<sup>2</sup>. The entire Andromeda galaxy, M32 and NGC 205 can be imaged with one pointing (as shown in the figure). The underlying M31 image is a single  $r_{P1}$ -band frame, which was chosen to have relatively small masked area. The masked areas (in black) visible e.g. in the detector 14 (marked in blue) are due to ill-functioning orthogonal transfer arrays (OTAs), video guide star data and areas on the focal plane with sub-standard imaging performance within this detector. These gaps can only be closed by large dithering or by rotating the camera.

Table 1: PAndromeda integration times in  $r_{P1}$ - and  $i_{P1}$ -bands for the 2010 season

Filter	Nights*	Images	Total integration time
$r_{P1}$	90(74)	1179	70740s
$i_{P1}$	66(56)	603	36180s

\*The number of nights with 2 visits are indicated in the parenthesis.

From the data header information one can see that each of the two nightly observing blocks yielding 12 frames with 60 seconds of exposure in 2 filters needs 16.2 minutes of telescope time. The overhead of about 35 percent includes the 13 seconds of read-out time, 15 seconds for filter change and about 30 seconds for focusing after a filter change. Due to the overhead for filter changes we requested to take only data in the  $r_{P1}$  and  $i_{P1}$  filters in 2010. The  $r_{P1}$  and  $i_{P1}$  filters are chosen because the source of the microlensing events are expected to be red evolved stars and the contamination from intrinsic variables in M31 is less severe in the  $r_{P1}$  filter.

Note that the central part of the camera close to the bulge of M31 is slightly out of focus (see Fig. 1).

For each filter, the observations within one visit have a polygonal dithering pattern with a radius of  $9''$ . It is either a hexagon ( $r_{P1}$ -band) or a square ( $i_{P1}$ -band) with the pointings located at the edges and the center.

### 3. Data processing

All images obtained for the PAndromeda project are processed through the Image Processing Pipeline (IPP) (Magnier 2006). The IPP runs the images through a succession of stages, including bias and dark correction, masking and artifact removal, flat-fielding, astrometric calibration (Magnier *et al.* 2008) and a flux-conserving warping (the images are resampled to a common pixelscale) to a sky-based image plane, so-called skycells. In the following we use the term “image” for the warped skycells.

The warped images have a dimension of  $6000 \times 6000$  pixels and a plate scale of  $0.2''/\text{pixel}$  which is smaller than the natural plate scale of  $0.258''/\text{pixel}$  of the PS1 Giga Pixel Camera. Each image has an attached variance map and a 16-bit mask image. For the PAndromeda project all images provided by the IPP are further processed using the PAndromeda data reduction pipeline. This pipeline is based on the difference imaging technique (Alard & Lupton 1998; Gössl & Riffeser 2002) which provides high precision photometric measurements in



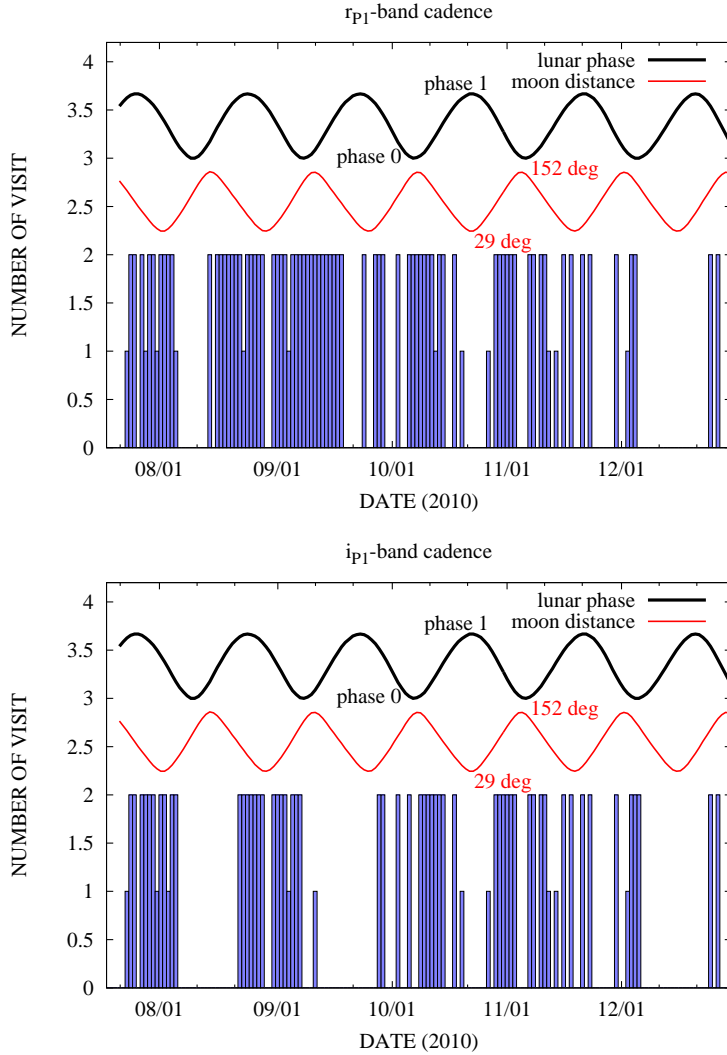


Fig. 2.— PAndromeda observation cadence. The histogram shows the number of visits (0, 1 or 2 times per night) on M31. The black line indicates the lunar phase (1 for full moon and 0 for new moon). The red line shows the distance of the M31 center from the moon as a function of observing date. A pause in the observations is visible in December when we were reaching the limit of the 2% PS1-time.

highly crowded fields. The PAndromeda pipeline has been integrated by us into the AstroWISE data management system (Valentijn *et al.* 2007) which has been developed to serve surveys with large data volumes. For a detailed description of the AstroWISE integration of our software we refer to Koppenhoefer *et al.* (2011).

In the following we describe each processing step that is performed by the PAndromeda

pipeline starting with the warped images until the creation of the light curves and the detection of microlensing events. Fig. 3 gives an overview of the different processing steps. These steps are performed independently for each filter  $r_{P1}$  and  $i_{P1}$  and for each skycell.

At the end of this section we analyze the astrometric and photometric stability of the light curves (see section 3.9 and section 3.10).

### 3.1. Interface between IPP and the PAndromeda Pipeline

By default the IPP subtracts the background in each warped image using a bi-linear interpolation of a model with coarsely sampled super pixels. The procedure works well in case of pure sky background. In the PAndromeda survey, however, the images contain also astrophysical background, i.e. the brightness profile of M31 which is one of the largest objects on the sky. In the PAndromeda pipeline the brightness profile is actually used later on. Therefore we requested to restore the background by the IPP that originally had been subtracted.

In the first data release the skycell layout used for the processing of the PAndromeda data was not optimized. In particular it does not make use of the fact that the detector boundaries are more or less the same with respect to M31 in each image. In some months from now a reprocessing of the PAndromeda data will be done by the IPP with skycells that are aligned with the outlines of the detectors.

Although not yet optimal, the processing used for this work is still good enough for the detection of microlensing events. In total we obtained 70 skycells with acceptable filling factor. We require at least 50% of each image not to be empty, to save disk space and computation time by avoiding images with large empty areas. One example, skycell 077, is shown in Fig. 4. Each skycell contains pixels of 4 different detectors in the current layout. In order to save disk space and to speed-up processing we apply a  $2 \times 2$  pixel binning to all images. In this way we are able to produce the light curves of a significant fraction of the total FOV of the first season data within a few weeks of computing time. In the future (i.e. when all previously taken PS1 images will be reprocessed with an improved Image Processing Pipeline) we will switch to the natural plate scale of  $0.258''/\text{pixel}$ .

In the first processing step of the PAndromeda pipeline all images are registered to the AstroWISE system, a procedure during which the IPP variance map and IPP mask images are merged into a single file - a variance map with zero values for masked pixels. The IPP variance maps have correlated noise. Due to remapping and reduced pixel size this correlated



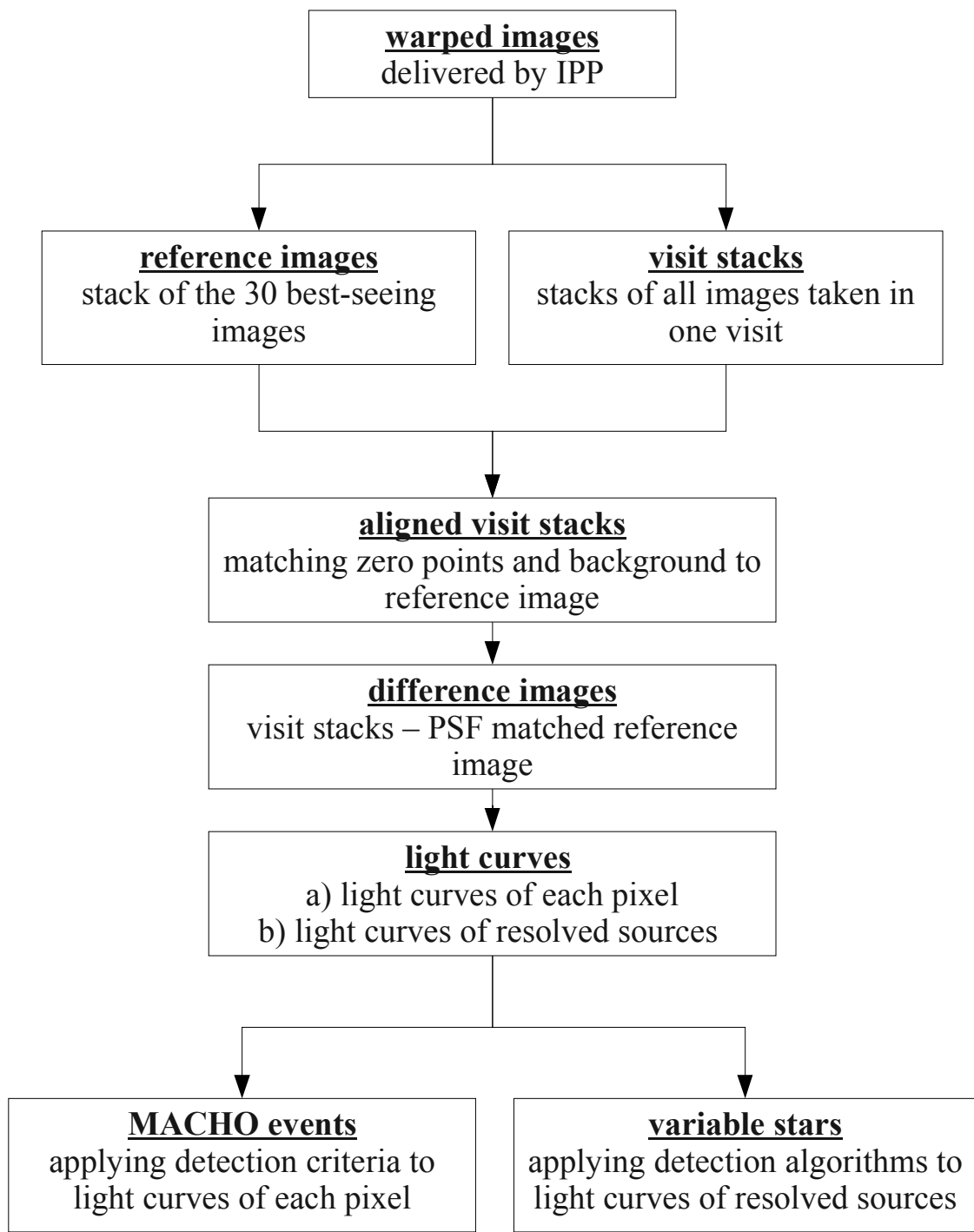


Fig. 3.— Overview of the processing steps performed by the PAndromeda data reduction pipeline for each sky cell.

noise is not accounted for in our pipeline, but we empirically correct for this by rescaling the error bars of the PSF light curves. (see section 3.7).

The PSF FWHM of each image is determined using the median of all FWHM\_IMAGE values measured by SExtractor (Bertin & Arnouts 1996). In addition we apply a filtering algorithm (Gössl & Riffeser 2002) to detect and mask cosmic rays based on their narrow FWHM.

### 3.2. Creation of a Reference Image

The difference imaging technique requires the creation of a reference frame which is a stack of the images with the best image quality. In our case we select the 30 best seeing images for each sky cell excluding images with a high masking fraction and/or a low transparency. We create a reference image in  $r_{P1}$ -band and  $i_{P1}$ -band for each sky cell. The individual processing steps are as follows:

In the first step we photometrically align each of the 30 input images  $I_i$  to the image with the very best seeing  $I_1$ . To account for zeropoint differences we multiply each image with a scaling factor  $f_i$ . Furthermore we add a model  $B_i$  to account for differences in the sky background:

$$I'_i = f_i \times I_i + B_i \quad . \quad (1)$$

For a proper photometric alignment of the single images, it is very difficult to calculate the scaling factor using a set of reference stars. In order to make use of all pixels in the field of view and to deal with the high crowding, each scaling factor  $f_i$  is calculated with the difference imaging technique: using all unmasked pixels of the image we calculate an un-normalized convolution kernel that would match the PSF of image  $I_1$  to image  $I_i$  and would simultaneously scale image  $I_1$  to the flux level as image  $I_i$ . We do not use the kernel to really convolve the images but rather calculate its inverse norm which delivers us the scaling factor  $f_i$ . In this way all scaled images  $I'_i$  have the same zero point but the PSF remains unchanged. Note that because the sky background in image  $I_i$  is still differing from the sky background in image  $I_1$  at this stage, we need to account for a sky background change while doing the calculation of the kernel. This is done with including a 1st order polynomial background in the minimization procedure.

The polynomial background is very robust when calculating the scaling factor  $f_i$ , however, for doing a proper adjustment of the sky background we do not use it and calculate a bicubic spline model  $B_i$  which has  $16 \times 16$  nodes with a separation of 183 pixel. The spline values at each grid point are calculated in the following way: first we apply a  $61 \times 61$  binning

to the scaled images  $f_i \times I_i$  (excluding all masked pixels) and subtract the binned images from the binned version of  $I_1$ . The subtracted images have a dimension of  $49 \times 49$  pixel and are then convolved with a  $3 \times 3$  median kernel resulting in an array of  $16 \times 16$ . These values are taken as the spline values at the grid points which are used to calculate the sky background correction  $B_i$ . After the photometric alignment all images have the same zeropoint and sky background.

Recently, Kerins *et al.* (2010) found that image subtraction in M31 works better when first performing a careful photometric alignment prior to matching the PSF. Although developed completely independent, our procedure is very similar. The difference of our method with respect to Kerins *et al.* (2010) is that we account for PSF differences when doing the photometric alignment.

The reference image is a weighted stack of all 30 photometrically aligned images where the weight,  $\alpha_i$ , for each image is calculated based on the background noise (median of  $\sigma$  in each pixel) and the PSF FWHM, as measured by SExtractor during the image registration:

$$\alpha_i = 1/(\sigma_i \times \text{FWHM}_i)^2 \quad . \quad (2)$$

Before stacking we replace masked pixels in each input image with the pixel values of the other image which has the most similar PSF. The similarity of the PSF is determined using a set of isolated stars. If a pixel is masked also in the most similar image, we replace with the second most similar image and so on. The procedure to replace masked pixels results in a very homogeneous PSF in the stacked image which is essential for the following processing steps. Note that this method only works if the set of input images already has similar PSFs. Fig. 4 shows an example reference image of skycell 077 in  $r_{P1}$ -band. The median PSF FWHM of all 30 input images is  $0.861''$  with  $\text{RMS} = 0.012''$ . In order to obtain the reference fluxes of all resolved stars in the reference image we subtract a bicubic spline model and perform PSF photometry on each source in the background subtracted image. The source positions are taken from a SExtractor table that has been created with the parameters `DETECT_THRESH=3` and `DETECT_MINAREA=5`. We iteratively subtract neighboring stars to remove blending effects (similar to the program DAOPhot, Stetson 1987). The reference fluxes will be added at a later stage to the fluxes measured in the difference images in order to create the light curves of resolved stars (see section 3.6).

### 3.3. Creation of a stack for each visit

Each visit of M31 consists of (up to) 7 individual exposures in  $r_{P1}$ -band which are obtained in a dithered mode. For some visits we also obtained (up to) 5 individual exposures

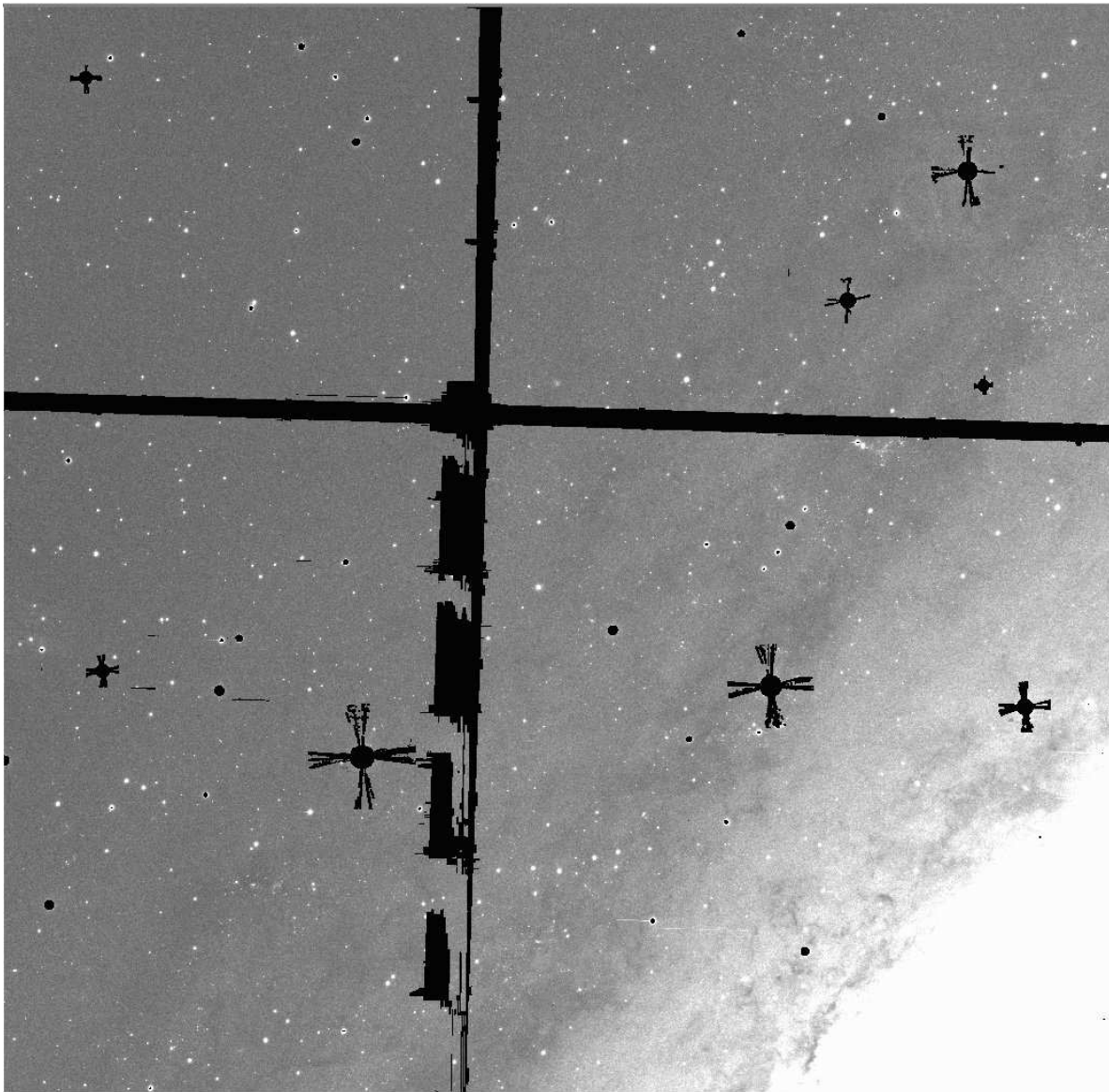


Fig. 4.— Reference image of skycell 077 in  $r_{P1}$ -band. The skycell contains pixels from 4 adjacent detectors with the vertical and horizontal masked area being the gap between them. Note that the layout of the skycells has not been optimized for the PAndromeda survey. In the future we will use skycells that are aligned with the detector borders. Each skycell image has a size of  $20' \times 20'$ .

in  $i_{P1}$ -band (see section 2). The single exposures of each visit are combined to a visit stack for each filter in order to improve the S/N and to eliminate masked areas. The procedure to create visit stacks is identical to the procedure described in the previous subsection. Also here, masked pixels in one image are replaced by the pixel values of the image with the most similar PSF. Note that although the number of input images is lower than in case of the creation of the reference images the requirement of finding an image with similar PSF is satisfied since all images of one visit are taken subsequently after focusing the camera in the beginning of the visit.

### 3.4. Photometric alignment

The single visit stacks are photometrically aligned to the reference image using the same procedure we described in section 3.2. After this step the visit stacks and the reference image have the same zeropoint and sky background and differ only in depth and PSF. Note that this zeropoint has an arbitrary value and only relative fluxes are calibrated. An absolute photometric calibration is done *a posteriori* as described in section 3.6.

### 3.5. PSF alignment and image subtraction

For each single visit stack we subtract a PSF aligned reference image and obtain a difference image. The PSF alignment is done using the standard approach proposed by Alard & Lupton (1998) with an optimal convolution kernel modeled as the superposition of a set of Gaussian kernel base functions which are modulated by a two-dimensional polynomial function in the x- and y-direction. We use the standard kernel model with 4 base functions having standard deviations of 9, 6, 3 and 0.1 pixel and a polynomial order of 2, 4, 6 and 0 respectively. The kernel is normalized (flux conserving) and has a size of  $51 \times 51$  pixel. The total number of free parameters is 50. In order to account for PSF variations across the skycell we divide the image into  $8 \times 8$  sub-fields and calculate a convolution kernel for each sub-field separately. Our procedure is similar to Kerins *et al.* (2010). The same procedure is also used for the WeCAPP data-set (Riffeser et al. in prep.).

The difference images contain only noise at the positions of constant sources. Variable objects such as microlensing events or eclipsing binaries are visible as positive or negative PSF-shaped residuals. Fig. 5 shows an example difference image of the bulge region of M31 in which several variable objects are clearly visible. Note that in the bulge of M31 the stellar density is so high that a large fraction of the pixels contains variable sources.



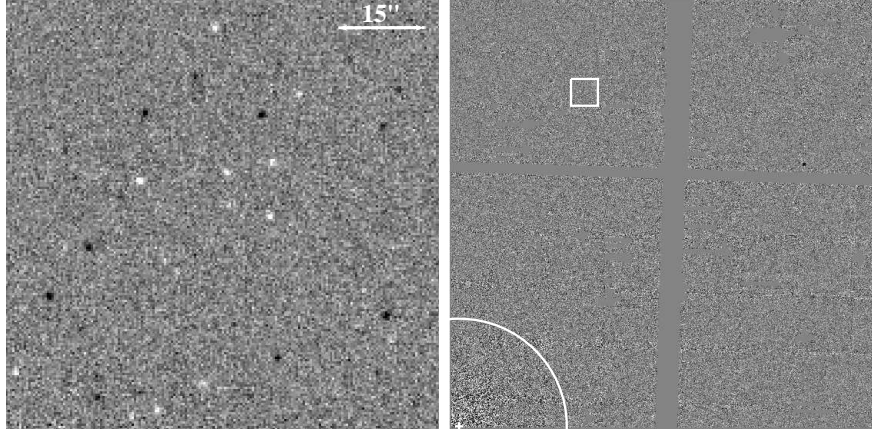


Fig. 5.— Zoom-ins to an example difference image of skycell 078 in  $i_{P1}$ -band. Left panel: Positive (white) and negative (black) residuals are visible at the position of variable sources. Right panel: The center of M31. The white circle indicates a distance of  $5'$  ( $1.12$  kpc) from the center of M31 (marked with the white cross). The vertical and horizontal masked area are the gaps between the detectors. The size of this image is  $20' \times 20'$ . The white box outlines the size of the zoom-in presented in the left panel. The flux cut-level of these two images are the same.

### 3.6. Creation of the light curves

The light curves are created using PSF-photometry on the difference images. The PSF is constructed using a set of isolated stars in the convolved reference image. The pixels of each PSF reference star are subdivided into a sub-pixel grid, shifted and combined. Since the stars are all on different sub-pixel positions, we obtain a smooth profile for the combined PSF with sub-pixel precision. The PSF is then used to measure the flux in each difference image after binning to the actual sub-pixel position of each star.

As shown in Fig. 3 we produce two sets of light curves. On the one hand we create a light curve of each pixel which we use for the detection of microlensing events. These light curves only contain differential fluxes as measured in the difference images. On the other hand we create light curves of resolved sources both in M31 and in the foreground. For those light curves we add the flux as measured in the reference image (see section 3.2) to the differential fluxes and obtain absolute fluxes.

### 3.7. Flux calibration

The flux calibration requires an existing catalog with similar filter as PS1. Thus we use the catalog of Data Release 7 from SDSS-II (Abazajian *et al.* 2009). The  $r_{P1}$  and  $i_{P1}$  are rather close to the SDSS analogs thus the overall flux calibration should be insensitive to color terms (Tonry *et al.* 2012). The data used consist of the M31 footprints Run 3356, 3366, 3367, 6426 and 7210 with a total of 6061956 sources. We calibrate our instrumental magnitude ( $m_{instr,PSF}$ ) in the reference image to the SDSS magnitude ( $m_{SDSS}$ ) with the following formula:

$$\begin{aligned} m_{SDSS} &= m_{instr,PSF} + ZP_{PSF} \\ &= -2.5 \log(F_{ref}[PSF_{ref}]) + ZP_{PSF} \end{aligned} \quad (3)$$

where the  $F_{ref}[PSF_{ref}]$  is the flux of a source determined with the PSF of the reference image  $PSF_{ref}$ . Note that the PSF profile and the amplitude is arbitrary and thus different in each sky cell. This is because the reference images are created out of 30 images having the best seeing, which do not necessarily have the same timestamp. The PSF profile is measured with selected stars on the reference image.  $ZP_{PSF}$  takes into account the difference between the SDSS magnitude and  $m_{instr,PSF}$  and also depends on the exact PSF-construction (how many and which stars are used, which kind of data enter the reference image). The flux calibration is performed on the reference images instead of the individual image, because the reference images have the highest S/N.

Each difference image is calibrated to have the same flux unit as the reference image and therefore

$$m_{SDSS} = -2.5 \log(F_{ref}[PSF_{ref}] + \Delta F_{diff}[PSF_{diff}]) + ZP_{PSF} \quad . \quad (4)$$

holds. This is very useful to determine the magnitude of variables. In an extreme case, the magnitude of a transient event which has not been detected before ( $F_{ref}[PSF_{ref}] = 0$ ) can be easily determined from the flux in the difference image alone.

The relative calibration of PS1 data with SDSS data in the  $i_{P1}$  and  $r_{P1}$  bands does not take into account color terms, but still is fairly accurate. The reason for this is that these color terms are small in the  $r_{P1}$  and  $i_{P1}$  filters (see Tonry *et al.* 2012). At a later stage we will nevertheless calibrate our PAndromeda data using PS1 calibration tools and data directly. In case the reader is interested in the magnitude transformation to the Johnson/Kron-Cousins  $BVRI$  system, we refer to the work by Ivezić *et al.* (2007):

$$\begin{aligned} R - r_{SDSS} &= -0.0107(r_{SDSS} - i_{SDSS})^3 + 0.005(r_{SDSS} - i_{SDSS})^2 - 0.2689(r_{SDSS} - i_{SDSS}) - 0.154 \\ I - i_{SDSS} &= -0.0307(r_{SDSS} - i_{SDSS})^3 + 0.1163(r_{SDSS} - i_{SDSS})^2 - 0.3341(r_{SDSS} - i_{SDSS}) - 0.3584 \end{aligned} \quad (5)$$



with the root-mean-square scatter for residuals evaluated for all their sample stars to be 15 millimag in  $R - r_{SDSS}$  and 19 millimag in  $I - i_{SDSS}$ .

Our single frame data are remapped twice: there is a remapping to the sky tessellation where the pixelsize is decreased. Later on when the single frame prereduced data from IPP (Sect. 3) get ingested into our pipeline the images are rebinned to twice the pixelsize (Sect. 3.1). The remapping causes a correlated noise depending also on the interpolation method used. Whereas our pipeline uses per pixel error propagation for all steps that are done after ingestion into our pipeline, it does not account for correlated noise that comes from the resampling before. We therefore empirically rescale the errors in the lightcurves directly, such that the formal PSF flux errors match the scatter of the PSF flux measurements. This rescaling factor is (as expected) the same for every skycell and every filter.

### 3.8. Microlensing event detection

The microlensing event detection is performed on the light curve of each pixel with successive criteria. The applied criteria for detection are as follows. For a preselection, we require at least three successive flux measurements in the light curve to be  $3\sigma$  above the base-line in either  $r_{P1}$  or  $i_{P1}$ -band. We then perform a microlensing fitting with the following formula (see Riffeser *et al.* 2006)

$$\Delta_F(t) \approx F_{\text{eff}} \left[ \frac{12(t - t_0)^2}{t_{\text{FWHM}}^2} + 1 \right] + a_0 + a_1(t - t_0) \quad (6)$$

where  $F_{\text{eff}}$  is the effective flux and for high magnifications is similar to the flux excess

$$F_{\text{eff}} := \frac{F_0}{u_0} \approx \Delta_F \quad , \quad (7)$$

$t_0$  is the time of flux maximum,  $t_{\text{FWHM}}$  is the full-width half-maximum event timescale.

The term  $a_0$  takes into account the shift of the base-line flux by a constant in cases for which there is a variable spatially close to the microlensing event and data of these variable phases enter the reference image. The term  $a_1$  is to include the gradient in the base-line flux in case the base-line flux is influenced by a long period variable close to the microlensing event. We require the data point closest to the time of the fitted maximum to have a good PSF.

We then filter out light curves with a  $\chi = \sqrt{\chi_{\text{dof}}^2}$  (where  $\chi_{\text{dof}}^2$  is the total  $\chi^2$  divided by the degree of freedom) larger than 1.4 in  $r_{P1}$ -band. We also require the S/N of the closest flux measurement to the time of the fitted maximum to be larger than 9 in both  $r_{P1}$  and  $i_{P1}$ -band.

The light curve of a microlensing event consists of many noisy data points that scatter around the baseline if one excludes the small time interval (of order  $2 \times t_{\text{FWHM}}$ ) where the microlensing event is measurable. The frequency of the deviations from the baseline depends on their amplitude and they occur at a rate given by the statistics of the PSF-flux errors. These deviations should be spread over the survey time and not be clustered in some time intervals. A correlated deviation from the baseline can be a hint of a nearby variable source or a time correlated artefact of data reduction. We would like to identify such correlations in the light curves and sort out microlensing candidates that have a good light curve fit but a signature for a time correlated deviation from the baseline not connected to the microlensing event.

The  $\chi^2_{\text{dof}}$  value of a light curve fit only tells how well a model describes the data averaged over all data points, but it is not sensitive of “how” the  $\chi^2$  contributions are spread over the data points, i.e. the survey time interval. We therefore add another criterion that quantifies the temporal correlations of the model mismatch. We define the model mismatch or deviation vector  $d_i = f_i - f(t_i)$  where  $f_i$  is the  $i$ -th flux measurement at time  $t_i$  and  $f(t_i)$  is the model flux at time  $t_i$  according to equation (6). The number of data points is  $n$ . With the further definition of  $s_i = \text{sign}\{d_i\}$ , so that  $s_i = 1$  or  $s_i = -1$  holds, we introduce

$$E_n = \sum_{i=1}^{n-1} s_i s_{i+1} \quad . \quad (8)$$

$E_n$  is a measure of how strongly the deviations of the data from the model are correlated in time. This equation is known also as the energy of a Lenz-Ising model (Ising 1925) with nearest neighbor spin interactions only.  $s_i$  is then the spin, and the spin-spin coupling constant usually called  $J_{ij}$  is equal to minus one in our case. In neuroscience the Ising model is often used to describe the energy of an ensemble of neurons (Tang *et al.* 2008) and this also our motivation for choosing such an extra term. Equation (8) quantifies (similar from our perspective) the “energy” for the deviations of data points from a model as seen by neurons.

For a random process, i.e. if the deviation vector  $d$  has no time correlation, the expectation value of equation (8) is zero. The distribution of  $E_n$  is gaussian with a width of  $\sqrt{n}$ . In order to make this scatter of  $E_n$  in equation (8) independent of the number of data points (similarly as the  $\chi^2_{\text{dof}}$  is independent of the degrees of freedom) we normalize equation (8) to

$$E = E_n / \sqrt{n} \quad . \quad (9)$$

We empirically require  $|E| < 3$  for the full light curve and  $|E_n^{\text{peak}}| < 3.5$  for the 20 flux measurements closest to the time of the flux maximum. We allow the time correlation of the deviation vector to be larger around the time of maximum brightness. This is purely

empirical. It can be justified by the need to allow for time coherent deviations from the points-mass-point-source standard model in the presence of extended sources and lenses, and disturbed deflection potentials. The criteria above (which are summarized below in Table 2) are not fine-tuned to pick some particular PS1 microlensing candidates but they were developed and tested for the WeCAPP project (Riffeser et al. in preparation).

If the energy criteria  $|E| < 3$  and  $|E_n^{\text{peak}}| < 3.5$  are fulfilled, we select the light curves with  $t_{\text{FWHM}}$  shorter than 20 days. This is to avoid the misinterpretation of long period variables as microlensing events due to the short time span of the first PAndromeda season. Contamination from the long period variables is less severe for campaigns with longer time span, e.g. the WeCAPP project (Riffeser et al. in preparation). All the criteria used are summarized in Table 2. All light curves that pass the microlensing event detection criteria are examined by eye. We exclude light curves for which the best-fitted maximum  $t_0$  and the time-interval plus/minus  $t_{\text{FWHM}}$  around the maximum are not in the time-span of the PAndromeda data-set (event time selection). We also exclude the light curves with the signature of variability outside the event timescale. The latter happens, e.g., when there are variables or artefacts close to the microlensing candidate that contribute some flux to the examined PSF light curve. The number of event candidates that are discarded after the event time selection is of the same order as the number of our final events. Thus our detection method is mostly automatic.

Table 2: Microlensing event detection criteria

	Criterion
I	Three successive $3\sigma$ flux measurement in $r_{\text{P1}}$ or $i_{\text{P1}}$
II	Good PSF around $t_0$
III	$\chi_{\text{dof}} < 1.4$ in $r_{\text{P1}}$
IV	$\text{S/N} > 9$ for maximum flux measurement in $r_{\text{P1}}$ and $i_{\text{P1}}$
V	$ E  < 3$ for the full light curve
VI	$ E_n^{\text{peak}}  < 3.5$ for measurements around $t_0$
VII	$t_{\text{FWHM}} < 20$ days

### 3.9. Astrometric precision of the warped images

In order to achieve high photometric accuracy with the image differencing technique it is very important to have a good alignment between the reference image and the single images - in other words to have a good relative astrometric calibration. In this section we

study the astrometric precision of the PAndromeda warped images and check the quality of the astrometry achieved by the IPP by calibrating against 2MASS.

As a first test we compare the x- and y-positions of sources in the  $r_{P1}$ - and  $i_{P1}$ -band reference images of skycell 068 (see Fig. 6). The RMS of the residuals is 175 mas (note that the distribution of residuals shows broad wings, and therefore the RMS value is dominated by large residuals. The standard deviation of a Gaussian fitted to the core of the distribution of residuals would be much smaller but this estimate strongly depends on the fitting radius). Further we check for systematic trends of the residuals as a function of position within the skycell (Fig. 7). There is no trend visible proving a homogeneous astrometric calibration.

The reference images have been constructed using the images with best image quality. In order to test if the internal astrometric calibration is good also for the rest of the data we compare the x- and y-positions of sources in two individual  $r_{P1}$ -band visit stacks, one of them having a very low airmass (1.07) and the other one having a high airmass (1.54). We find a somewhat lower precision (RMS of 237 mas) but no trend with position within the skycell.

We also tested the absolute astrometric precision comparing the positions measured in the  $r_{P1}$ -band reference images of skycell 068 with a catalog from SDSS DR7 (Abazajian *et al.* 2009). Here we see a systematic trend only at the sub-pixel level in the RA coordinate as a function of RA as well as a constant systematic offset of the DEC coordinates (see Fig. 8). We cannot say whether this points to a problem in the astrometric calibration done by the IPP or if the SDSS catalog has a calibration issue. In any case, for the quality of the light curves only the relative astrometric precision is important and since the offset is small compared to the pixel size we see no problems with identifying objects when cross-matching with external catalogs.

### 3.10. Photometric stability and quality of the light curves

To understand the data quality of PAndromeda, we first investigate two sub-fields, one in the bulge of M31 (skycell 077) and one in the disk (skycell 091). A histogram of the PSF distribution is shown in Fig. 9. The maximum peaks at  $1''$ .

To quantify the precision of the photometry, we perform a test on sub-fields in the bulge, disk and the astrometric fields. We use SExtractor to extract the position of the resolved stars in the reference images of the sub-fields and create the light curves, i.e. flux difference of these stars relative to the mean flux as a function of time, at the position of these stars with our PAndromeda pipeline. Since most of the stars are not variable, the scatter of

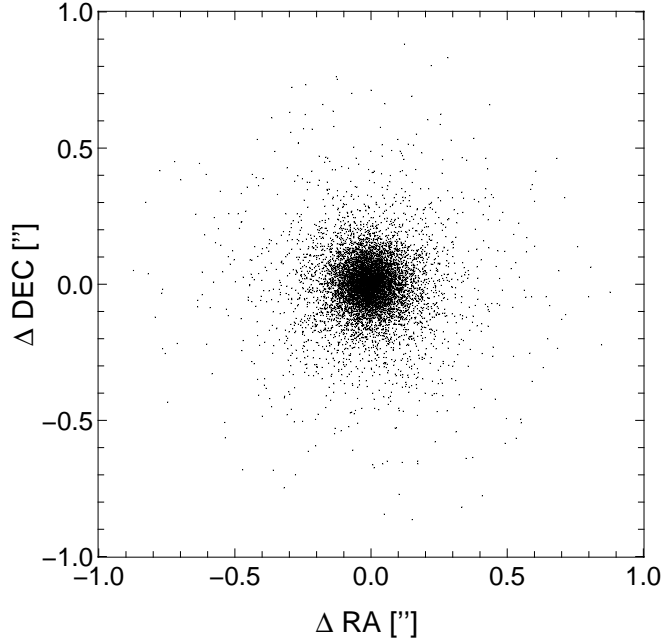


Fig. 6.— Internal astrometric precision measured by comparing the positions of all sources in the  $r_{P1}$ - and  $i_{P1}$ -band reference images of skycell 068.

the estimated flux difference (relative to the mean flux) is an estimate for the photometric precision as a function of the magnitude of the star. The ratio for this RMS-error relative to the stellar flux is plotted for each star in Fig. 10. In the plot we present the  $3\sigma$  clipped RMS value. The theoretical S/N predictions, account for the contributions from sky, read out, object and scintillation noise, are shown in the black lines. We assume the surface brightness of M31 in  $r_{P1}$  to be 20.5 and 21.5 mag/arcsec<sup>2</sup> at the location of skycell 077 and skycell 091 (Tempel *et al.* 2011). The RMS distributions from the data are shifted from the theoretical expectations. This is because masking is not taken into account. Besides, the resampling to the skycells and binning process also has influenced the quality of the light curves. Nevertheless, the result shows that the photometric precision is 1% for stars with  $r_{P1} = 19$  mag.

#### 4. Examples for variable light curves

We also analyze the light curves of the resolved sources in the central  $40' \times 40'$  sub-field. We find about 60 Cepheid-like sources by inspecting the light curves with large  $\chi^2$  when fitting a constant base-line. An example light curve is shown in Fig. 11. These Cepheid-like

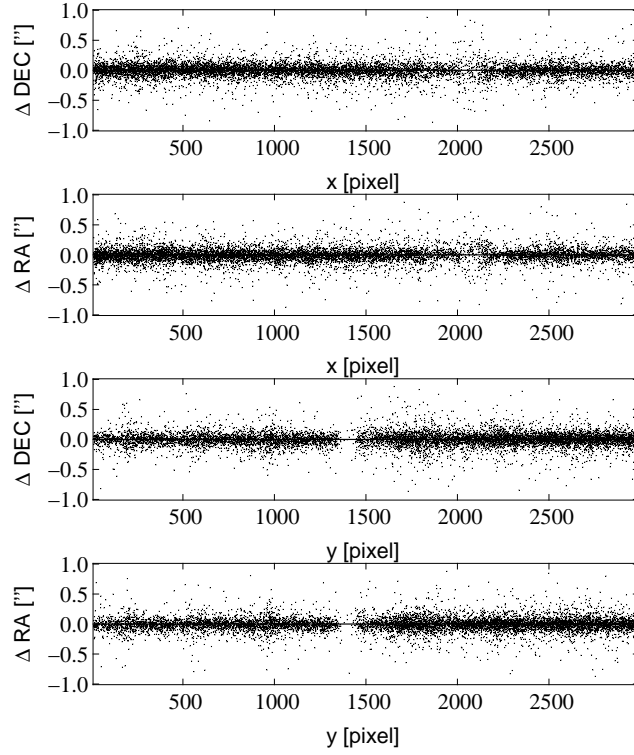


Fig. 7.— Same astrometric residuals as shown in Fig. 6 plotted as a function of position within the skycell. The gaps between the 4 detectors that overlap with this skycell are clearly visible (compare Fig. 4).

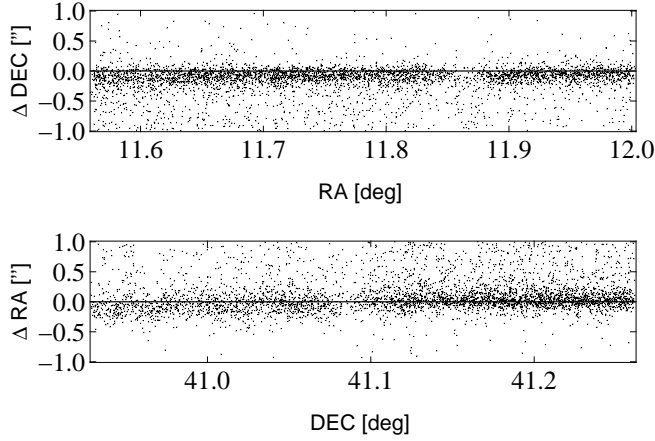


Fig. 8.— Absolute astrometric precision measured by comparing the positions of all sources in the  $r_{P1}$ -band reference images of skycell 068 to a catalog of the Sloan Digital Sky Survey DR7. There is a small offset in Declination and a trend in Right Ascension as a function of Declination. Both effects are at the sub-pixel level ( $\sim 0.1''$ ).

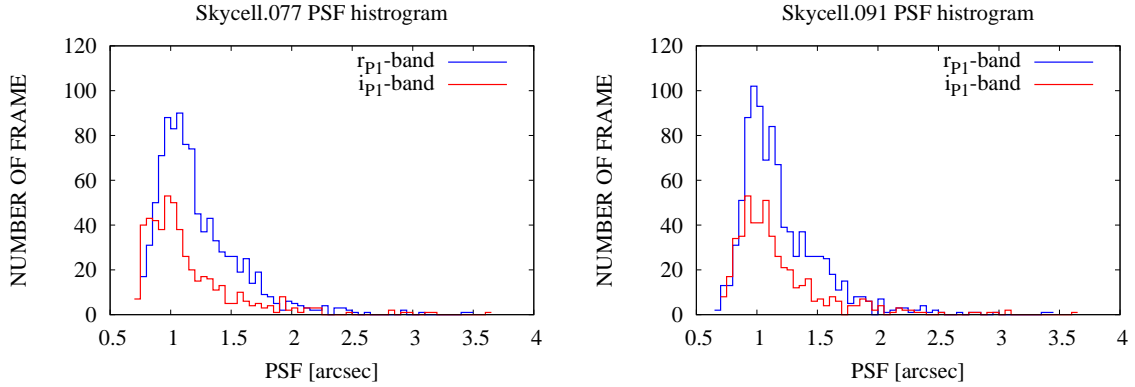


Fig. 9.— Point-Spread Function (PSF) distribution of the first season of PAndromeda in the bulge (left panel) and disk (right panel) field. The PSF distributions of the  $r_{P1}$  ( $i_{P1}$ ) data are shown in the blue (red).

sources and further candidates that will be found in the remaining M31 fields will be analyzed in a forthcoming publication (Gössl et al. in prep.). In addition, we find one eclipsing binary and present its folded light curve in Fig. 12.

During the time span of the first observing season of PAndromeda we find a few nova candidates in the central  $40' \times 40'$  sub-field. An example light curve is shown in Fig. 13.



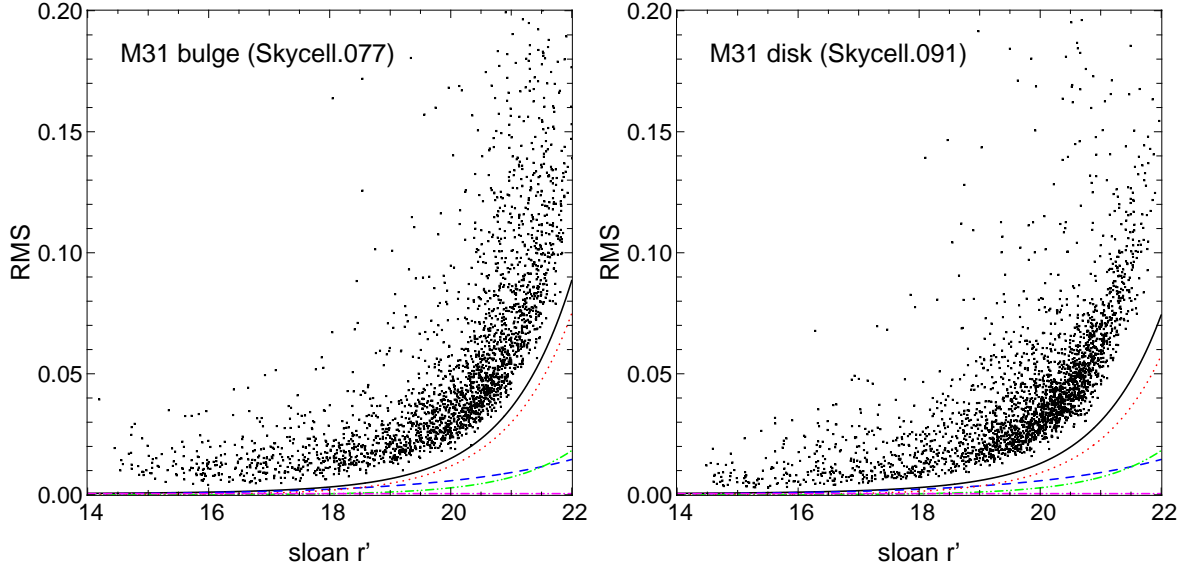


Fig. 10.— Percentage photometric accuracy (rms) as a function of the magnitude of stars from images taken by PAndromeda in the bulge field (left panel) and the disk field (right panel). The RMS is derived from the light curves of resolved stars. The black line is the expected total RMS, taking into account the contributions from sky (red line), read out (green line), object (blue line) and scintillation noise (magenta line).

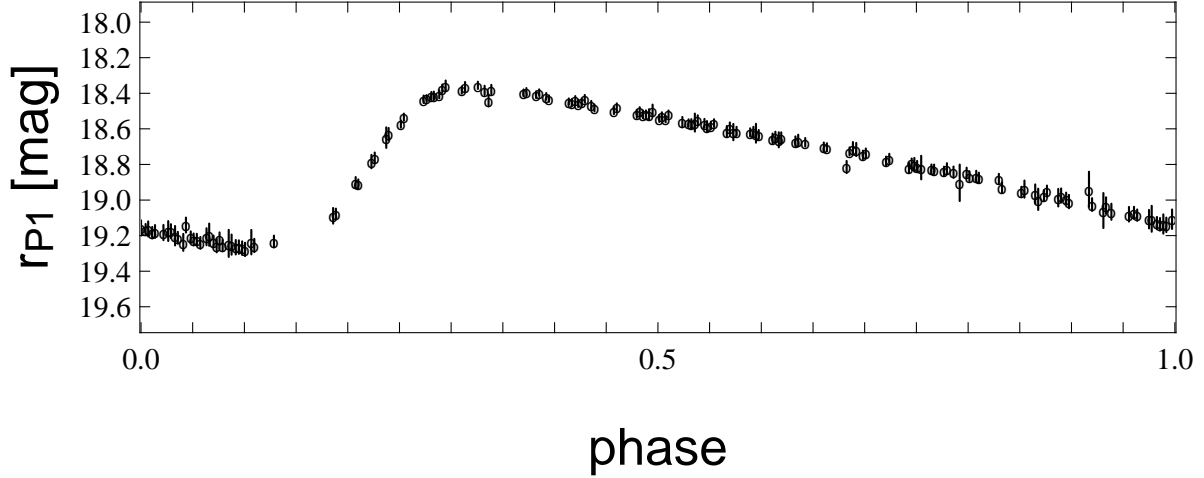


Fig. 11.— Folded  $r_{P1}$ -band light curve of our best Cepheid candidate at  $RA(J2000) = 10.2662$  deg and  $Dec(J2000) = 41.1512$  deg. The period is 45.6 days and the distance from the center of M31 is  $20'$ .

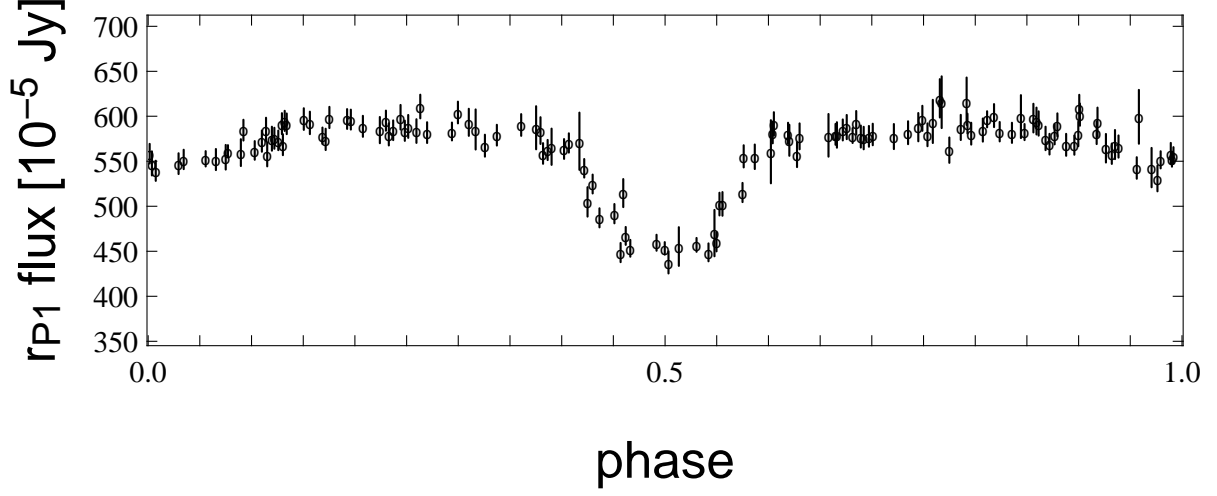


Fig. 12.— Folded  $r_{P1}$ -band light curve of a foreground eclipsing binary at  $\text{RA}(\text{J2000}) = 10.6698$  deg and  $\text{Dec}(\text{J2000}) = 41.1681$  deg. The period is 0.5 day.

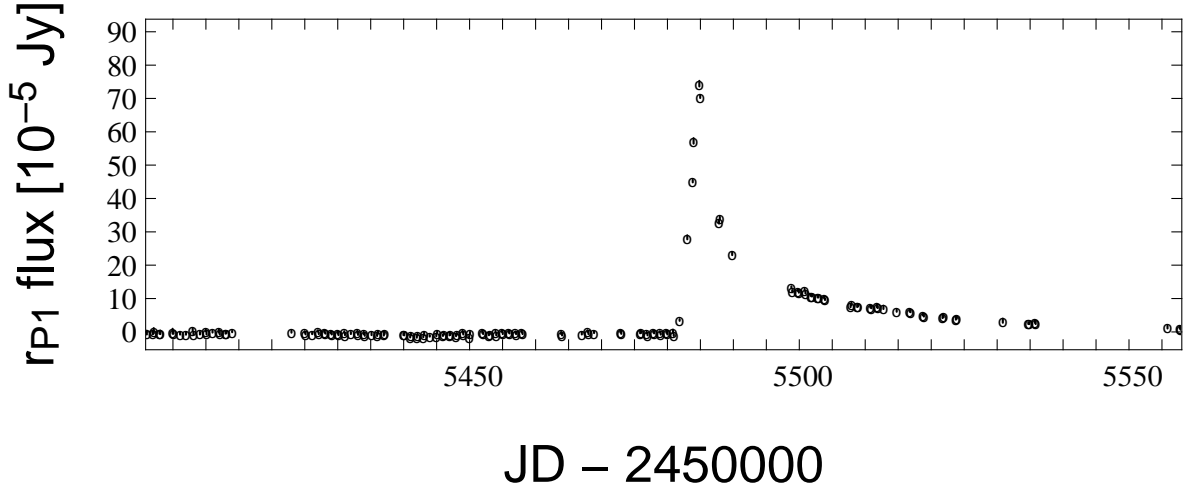


Fig. 13.—  $r_{P1}$ -band light curve of the nova M31N-2010-10c from PAndromeda survey at  $\text{RA}(\text{J2000}) = 11.1108$  deg and  $\text{Dec}(\text{J2000}) = 41.5205$  deg.

### 5. The first microlensing events

To compare with the previous results, we first analyzed the central region of the M31 field ( $40' \times 40'$ ) and detect 6 candidates. The positions and light curves of these 6 candidates are shown in Fig. 14, Fig. 15 and Fig. 16. The fitting parameters (as shown in equation (6)) and the  $\chi_{\text{dof}}$  are presented in Table 5.

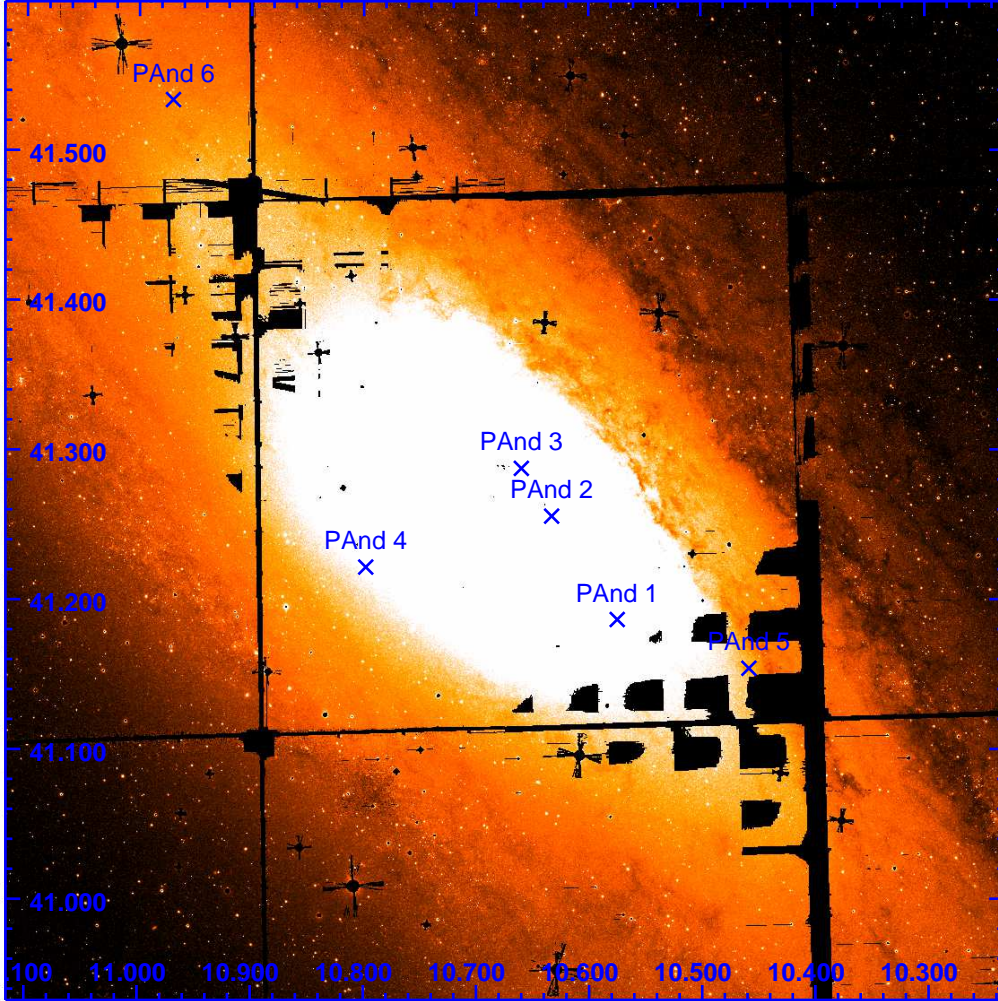


Fig. 14.— Position of the six microlensing event candidates detected in the central  $40' \times 40'$  region of M31 from PANDROMEDA. The coordinates, RA (J2000) in hour and Dec (J2000) in degree are also shown in the figure. The FOV of this image is  $40' \times 40'$ .

Table 3: PAndromeda microlensing event candidates in  $r_{P1}$  - and  $i_{P1}$ -band.

	IAU name	RA(2000) [h:m:s]	DEC(2000) [d:m:s]	$\Delta_{M31}$	$t_0$	$t_{FWHM}$ [day]	$F_{\text{eff},r_{P1}}$ [ABmag]	$F_{\text{eff},i_{P1}}$ [ABmag]	$(r_{P1} - i_{P1})^a$ [ABmag]	$\chi_{\text{dof},r_{P1}}$	$\chi_{\text{dof}}$
PAnd-1	PSO J010.5746+41.1872	00:42:17.9	41:11:14	10.0'	5479.05±0.04	1.28±0.09	20.52±0.05	20.29±0.06	0.23±0.10	1.1	1.1
PAnd-2	PSO J010.6329+41.2564	00:42:31.9	41:15:23	4.2'	5433.33±0.04	2.07±0.16	20.22±0.06	19.80±0.08	0.42±0.13	1.2	1.3
PAnd-3	PSO J010.6596+41.2883	00:42:38.3	41:17:18	2.3'	5451.49±0.04	3.34±0.14	18.95±0.03	17.60±0.05	1.35±0.08	1.4	1.9
PAnd-4	PSO J010.7979+41.2222	00:43:11.5	41:13:20	9.5'	5484.73±0.11	13.82±0.43	20.41±0.02	20.07±0.03	0.34±0.06	1.1	1.1
PAnd-5	PSO J010.4579+41.1547	00:41:49.9	41:09:17	19.3'	5498.05±0.17	9.04±0.36	20.92±0.04	20.18±0.05	0.74±0.07	1.2	1.4
PAnd-6	PSO J010.9700+41.5344	00:43:52.8	41:32:04	27.8'	5511.76±0.12	3.08±0.40	21.97±0.08	21.27±0.12	0.69±0.22	1.0	1.1

We give the IAU name of the 6 microlensing candidates in column 2, the coordinates in columns 3 and 4, the distance to the center of M31 ( $\Delta_{M31}$ ) in column 5, the time of flux maximum (JD - 2450000) and event timescale in columns 6 and 7 the maximum flux in units of magnitude in  $r_{P1}$  and  $i_{P1}$ -band in columns 8 and 9, the color in column 10 and the best-fitted  $\chi_{\text{dof}}$  in columns 11 and 12.

<sup>a</sup>The  $r_{P1}$  and  $i_{P1}$  are rather similar to the SDSS analogs (see Tonry *et al.* 2012, for further description.).

Table 4: PAndromeda microlensing event candidates with magnitudes in  $R$  and  $I$ -band.

	$F_{\text{eff},R}$	$F_{\text{eff},I}$	$(R - I)$
	[mag]	[mag]	[mag]
PAnd-1	20.10	19.86	0.24
PAnd-2	19.75	19.32	0.43
PAnd-3	18.21	16.93	1.28
PAnd-4	19.96	19.61	0.35
PAnd-5	20.36	19.63	0.73
PAnd-6	21.42	20.72	0.70

For readers who are used to the Johnson-Cousins system, we provide the magnitude and color in  $R$  and  $I$  from equation (5).

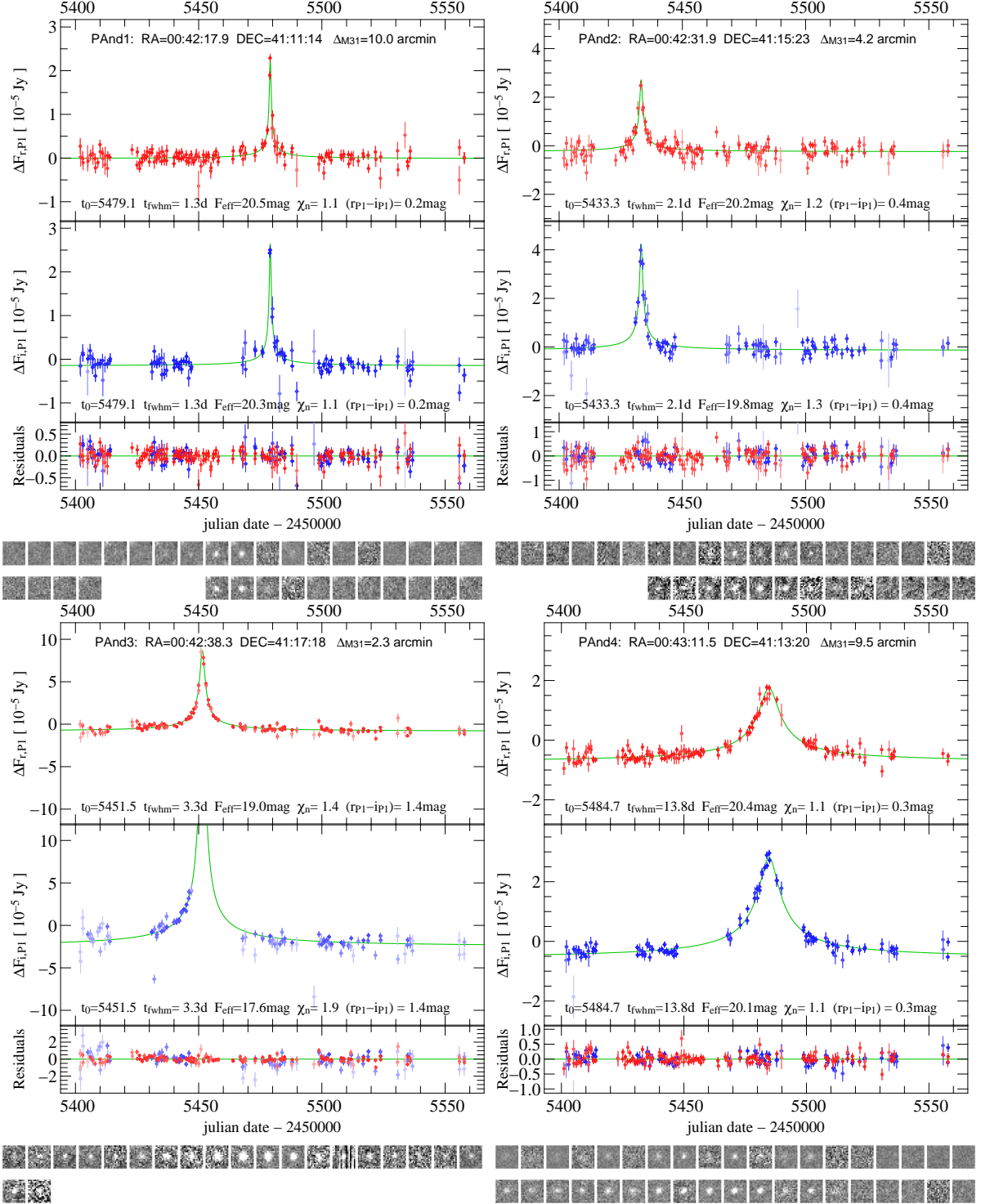


Fig. 15.— Light curves of the microlensing events detected in the central  $40' \times 40'$  region of M31 from PAndromeda. Upper (middle) panel shows the light curve in  $r_{P1}$  ( $i_{P1}$ ) and the lower panel shows the residuals to the best-fitted light curve. In the figure there are also the name of the event (e.g. PAnd-1), the coordinates  $\alpha$  (RA) and  $\delta$  (Dec) at the epoch of J2000, the distance to the center of M31 ( $\Delta_{M31}$ ) in arcminutes. The best-fit light curves (green) and parameters (black) are also shown, which are the time at maximum magnification ( $t_0$ ), the event timescale ( $t_{FWHM}$ ) in units of a day, the equivalent magnitude at maximum magnification ( $F_{eff}$ ) in mag, the chi-squared value ( $\chi_n$ ) and the difference in magnitude between the two bands ( $r_{P1} - i_{P1}$ ) in mag.

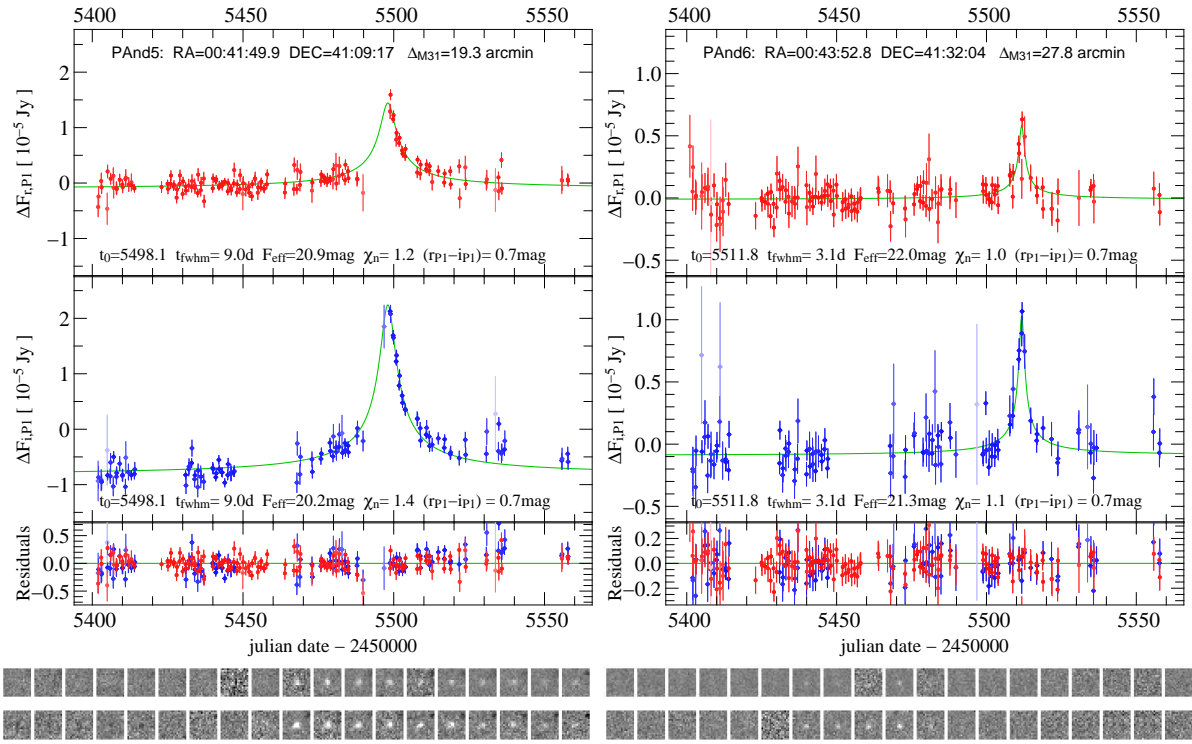


Fig. 16.— Light curves of PAnd-5 and PAnd-6. See the figure caption of Fig. 15 for further explanation.



The 6 PAndromeda events form 3 groups. PAnd-2 and PAnd-3 are at 4.2' and 2.3' (0.5-1.0 kpc) from the Andromeda center. This region will be bulge-bulge lensing dominated regardless of the halo-MACHO content. The colors ( $r_{P1} - i_{P1} = 0.4$  and  $1.4$  mag,  $R - I = 0.4$  and  $1.3$ ) and short time scales ( $t_{FWHM} = 2.1$  and  $3.3$  day) of the events are in agreement with bulge stars lensing post main sequence bulge stars (see Riffeser *et al.* 2006). The events PAnd-4 and PAnd-1 are at 9.5' and 10' distance from the M31 center along the minor and major axes (corresponding to  $\sim 2$  kpc). These are regions where the light profile turns from bulge light dominated to disk light dominated (compare, e.g. the Fig. A.1 of Tempel *et al.* 2011, for the  $g$ -band dust corrected minor and major M31 surface brightness profiles). Hence, the bulge-bulge and to a smaller degree the bulge-disk self-lensing rates are reduced relative to the center. On average the sources of self-lensing become more likely disk stars, and thus bluer. The timescales of self-lensing stay short, i.e. a few days. PAnd-1 has a timescale of 1.3 days, the other (PAnd-4) is considerably longer and has a timescale of 14 days. This is expected only for a very small fraction of self-lensing events (compare the density contours of Riffeser *et al.* 2006, Fig. 9) and is more easy to reconcile with halo lensing.

The events PAnd-5 and PAnd-6 finally are at 19.3' and 27.8' or 4.5 and 6 kpc from the M31 center along the major axis. This is the location where the SFB from the bulge drops to or below that of the young disk component, which is about 4 magnitudes below the SFB of the disk. At this distance from the M31 center bulge lensing should be almost zero and disk-disk self-lensing should be (because of the inefficient geometry due to the small line of sight extension) small as well. Halo lensing by MACHOs will decrease less fast out to 6 kpc since the disk stars provide a spatially almost 'flat' (compared to the bulge) resource for halo lensing at 2-6 kpc. The timescale of the two outer lensing events is 3 (PAnd-6) and 9 (PAnd-5) days. The colors are both 0.7 mag (in either  $r_{P1} - i_{P1}$  or  $R - I$ ), which is in agreement both with evolved bulge and disk stars. Since PAnd-5 is at a location where dust lanes become visible we also checked the extinction values along the line of sights to the events, to find out, whether one event could be particularly reddened by M31 dust. We used the dust extinction map of Montalto *et al.* (2009) (the spatial resolution of the dust map is 6''/pixel) and obtained  $E(B-V)$  values of 0.17 to 0.2 for all 6 events. According to this map PAnd-5 is close but not along the line of sight to a larger dust extinction.

Our results concerning these long timescale events at 2 and 6 kpc from the Andromeda center are in agreement with previous results: Long time scale lensing events have been found by POINT-AGAPE (Calchi Novati *et al.* 2005) at a distance of 22' from M31 (PA-99-N2) with a timescale of 22 days.

We also inspect the HST images at the location of these events (see Fig. 19). At this point we assume that the world coordinate system (WCS) of the HST images is correct and

we do not map them to the PS1 images. There are HST archive images for all the events except PAnd-5. At the position of PAnd-3, PAnd-4 and PAnd-6, there are one to several resolved sources around the position of our candidates, while for PAnd-2 there is a possible source and for PAnd-1 nearby sources can be ruled out.

We have not found extended sources (background galaxies) overlapping or close to our events, so we can rule out the contamination from SNe. This is also confirmed by the good  $\chi_{\text{dof}}$  from fitting the microlensing light curve.

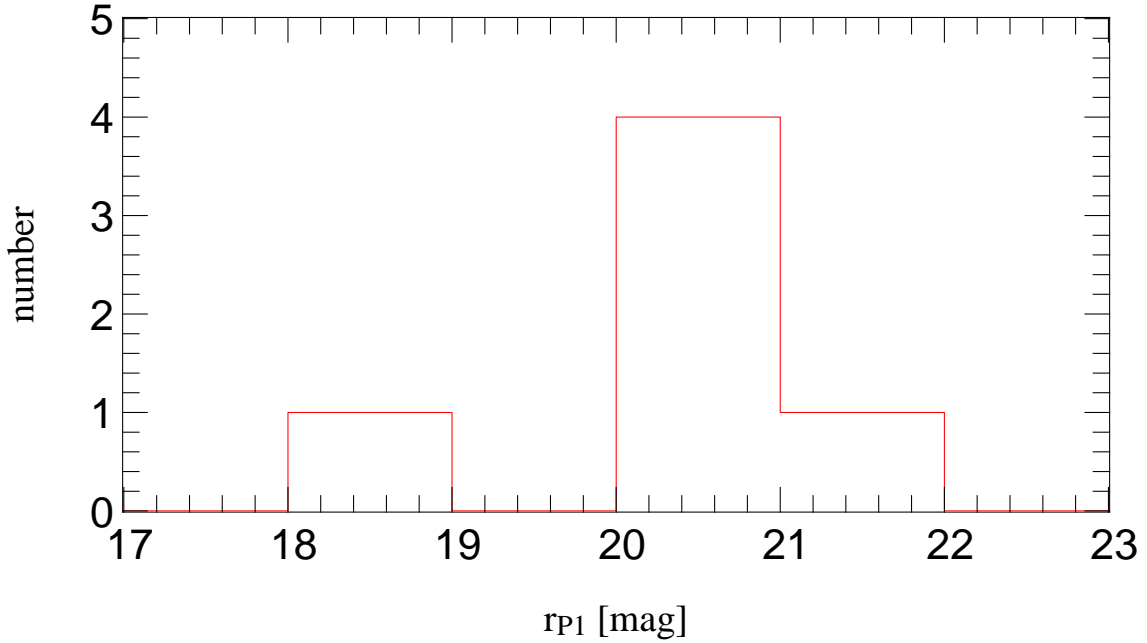


Fig. 17.— Distribution of the  $F_{\text{eff},r_{P1}}$  of the 6 PAndromeda microlensing events from Table 5. Most of the events have  $r_{P1}$  fainter than 20 mag at the flux maximum except PAnd-3. Such a bright event is hard to reconcile with self-lensing due to the flux excess limit caused by finite-source effects. In general very bright events can be more easily caused by MACHOs (Riffeser *et al.* 2008).

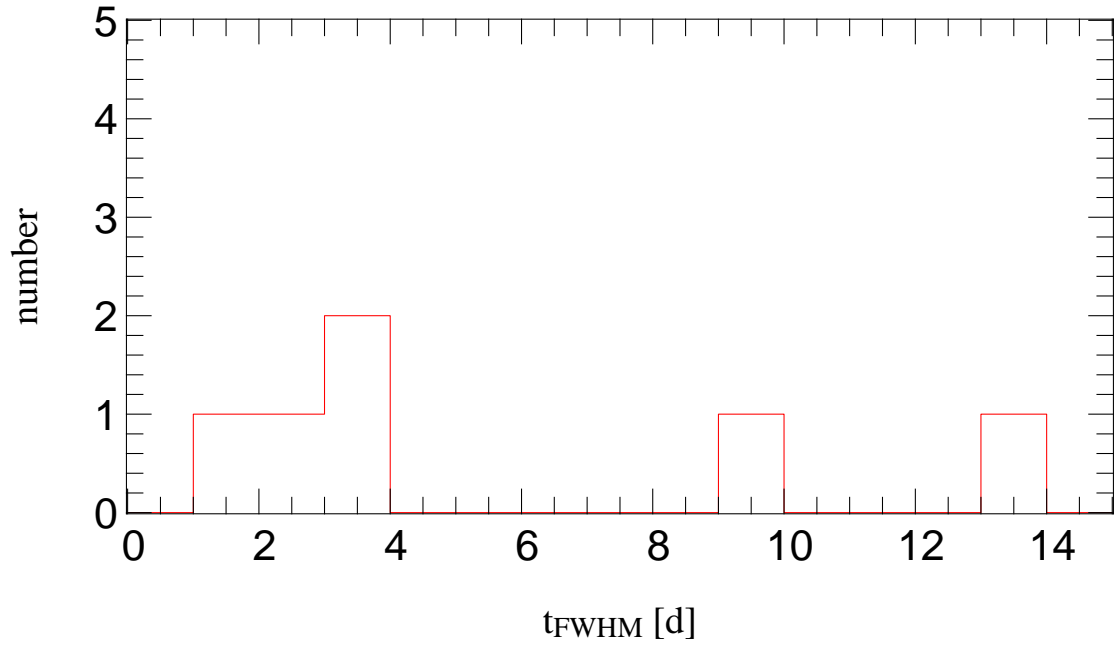


Fig. 18.— Distribution of the  $t_{\text{FWHM}}$  of the 6 PAndromeda microlensing events. The timescale of the detected events ranges from 1.3 to 13.8 days, with 4 out of the 6 events have  $t_{\text{FWHM}}$  below 5 days. This demonstrates that the PAndromeda survey is effective in finding short duration events.

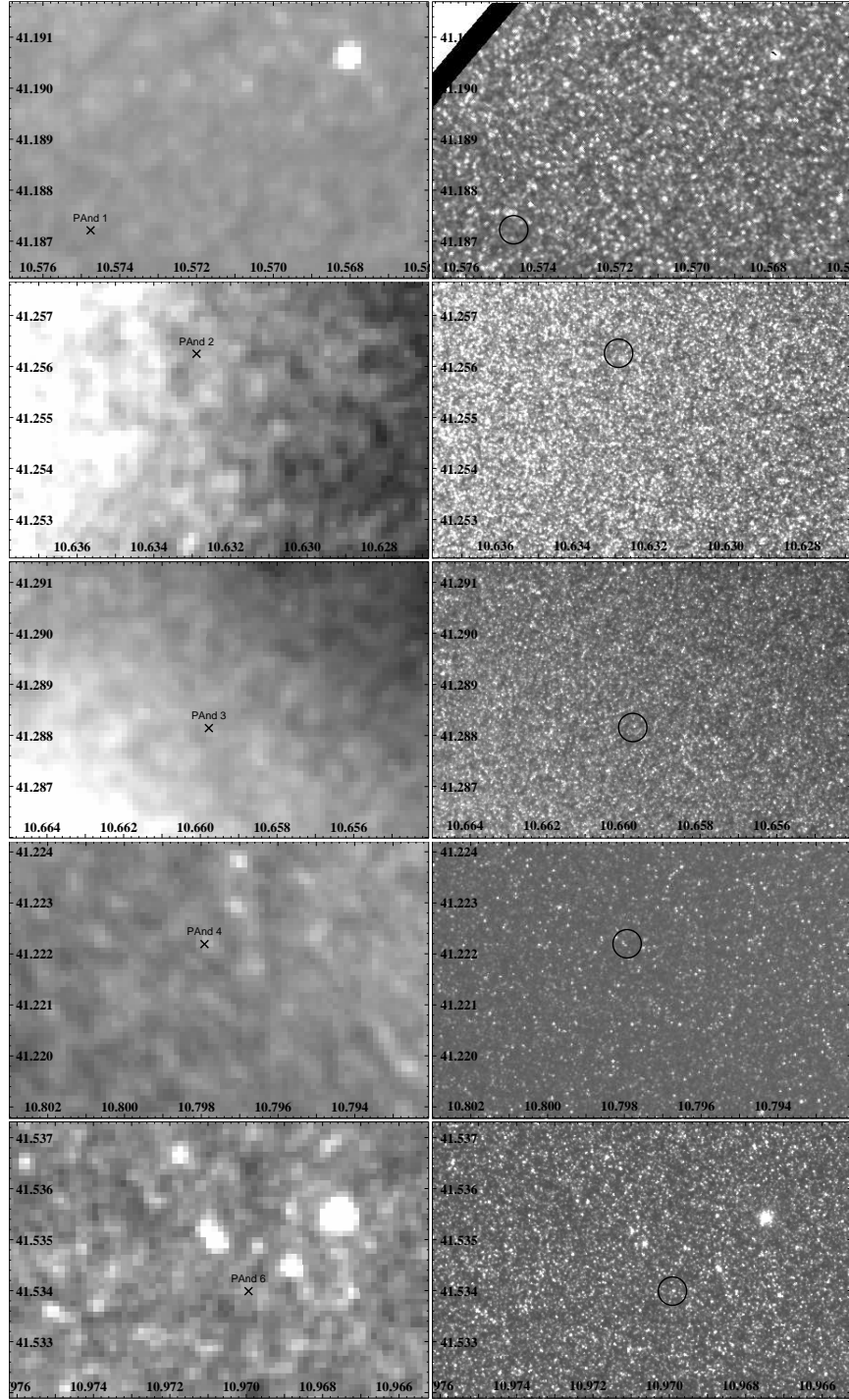


Fig. 19.— Comparison of PS1 images (left column) with the HST images (right column). The HST image of PAnd-1 is from a median of 3 ACS 814 nm archive data (u3d9020at\_drz.fits, u3d9020gt\_drz.fits, u3d9020mt\_drz.fits) of HST Cycle 5 proposal 6300 by Ford, H.. The HST image of PAnd-2, PAnd-3 and PAnd-4 are from ACS 814 nm archive data (jbf309010\_drz.fits, jbf308010\_drz.fits and jbf310010\_drz.fits) of HST Cycle 18 proposal 12058 by Delcanton, J.. The HST image of PAND-6 is from ACS 606 nm archive data (j96q05010\_drz.fits) of HST Cycle 13 proposal 10407 by Morrison, H..

## 6. Outlook

We are currently analyzing the full data set of the first PAndromeda season. Besides the point-source point-lens modeling and detection presented in section 5, a search for the finite-source effects according to the process by Lee *et al.* (2009) will also be carried out. Further investigations on the individual bright events following the analysis of Riffeser *et al.* (2008) will shed light on the identity of these events, whether they are more likely caused by MACHOs than by stellar lenses. A comprehensive study of the detection efficiency (e.g. as a function of  $\Delta_F$  and the event duration in the different fields) will also be done.

In addition to the microlensing analysis, we will use the PAndromeda data-set to improve the M31 model in several aspects, for example, including the dust content (Montalto *et al.* 2009), modeling the three-dimensional distribution of stars. At the time of writing this paper, we are also granted time to investigate the stellar population and dynamics of the M31 bulge in more detail (10 nights of the 2.7m telescope at McDonald observatory, with the VIRUS-W instrument), e.g. the bulge-bulge self-lensing (main contribution to the self-lensing in the center of M31) can be quantified at a much better level than now.

The IPP is going to deliver a reprocessing of the PAndromeda data in some months from now. We will analyze the reprocessed data and also the upcoming new data without binning. The observation strategy in 2011 is similar to 2010. We have two rotation angles of the de-rotator both with a good matching on a grid of corresponding detectors. In 2010 the stars on the central part of the cameras were defocused, leading to a decreased S/N. This can mimic an asymmetric microlensing signal. Therefore for 2011 we shift this defocused center to the major axis of M31 to have more symmetric signals from both sides of M31 (see Fig. 1). Of course, our final detection efficiency study will have to account for the varying PSF sizes in different sky cells.

In 2011 we continue with our two block strategy with a time gap of three to five hours accepting short offsets of <30 min due to scheduling constraints. The filters and exposure times will be the same like in the previous season.

The pointing follows a dither pattern with a diameter of 13'' to 20'' and a cycle of 5 images. This ensures that all the detector gaps are filled completely. The regular observations have started on 25th July 2011.

## 7. Conclusion

The preliminary analysis of the first part of the first season PAndromeda data demonstrates that one can indeed detect microlensing events at a competitive rate per season (see Calchi Novati 2010, for a summary of previous surveys and events). The data are further useful for novae detection and investigation of other variables.

The identification of 4 short-duration microlensing events with  $t_{\text{FWHM}} \sim 1\text{-}3$  days shows that the time resolution of the PAndromeda project is comparable with the best 2 seasons of the WeCAPP project (where two telescopes were coordinated to monitor M31). The advantage of PAndromeda is the capability to cover the entire M31 disk with one pointing (compared to the  $17.2' \times 17.2'$  FOV of WeCAPP). By finding or excluding microlensing events in the outer disk of M31, the PAndromeda survey will manifestly exceed the accuracy of previously derived M31-halo MACHO fractions.

### *Acknowledgments*

We thank for comments from the anonymous referee. We are grateful to Sebastiano Calchi Novati and Jelte de Jong for their useful comments. This work was supported by the DFG cluster of excellence ‘Origin and Structure of the Universe’ ([www.universe-cluster.de](http://www.universe-cluster.de)).

The Pan-STARRS1 Survey has been made possible through contributions of the Institute for Astronomy, the University of Hawaii, the Pan-STARRS Project Office, the Max-Planck Society and its participating institutes, the Max Planck Institute for Astronomy, Heidelberg and the Max Planck Institute for Extraterrestrial Physics, Garching, The Johns Hopkins University, Durham University, the University of Edinburgh, Queen’s University Belfast, the Harvard-Smithsonian Center for Astrophysics, and the Las Cumbres Observatory Global Telescope Network, Incorporated, the National Central University of Taiwan, and the National Aeronautics and Space Administration under Grant No. NNX08AR22G issued through the Planetary Science Division of the NASA Science Mission Directorate.

Funding for the SDSS and SDSS-II has been provided by the Alfred P. Sloan Foundation, the Participating Institutions, the National Science Foundation, the U.S. Department of Energy, the National Aeronautics and Space Administration, the Japanese Monbukagakusho, the Max Planck Society, and the Higher Education Funding Council for England. The SDSS Web Site is <http://www.sdss.org/>.

The SDSS is managed by the Astrophysical Research Consortium for the Participating Institutions. The Participating Institutions are the American Museum of Natural History, Astrophysical Institute Potsdam, University of Basel, University of Cambridge, Case Western Reserve University, University of Chicago, Drexel University, Fermilab, the Institute for Ad-

vanced Study, the Japan Participation Group, Johns Hopkins University, the Joint Institute for Nuclear Astrophysics, the Kavli Institute for Particle Astrophysics and Cosmology, the Korean Scientist Group, the Chinese Academy of Sciences (LAMOST), Los Alamos National Laboratory, the Max-Planck-Institute for Astronomy (MPIA), the Max-Planck-Institute for Astrophysics (MPA), New Mexico State University, Ohio State University, University of Pittsburgh, University of Portsmouth, Princeton University, the United States Naval Observatory, and the University of Washington.

## REFERENCES

- Abazajian, K. N., Adelman-McCarthy, J. K., Agüeros, M. A., Allam, S. S., Allende Prieto, C., An, D., Anderson, K. S. J., Anderson, S. F., Annis, J., Bahcall, N. A., & et al. 2009: *The Seventh Data Release of the Sloan Digital Sky Survey*, ApJS, 182, 543
- Alard, C. & Lupton, R. H. 1998: *A Method for Optimal Image Subtraction*, ApJ, 503, 325
- Alcock, C., Allsman, R. A., Alves, D. R., Axelrod, T. S., Becker, A. C., Bennett, D. P., Cook, K. H., Dalal, N., Drake, A. J., Freeman, K. C., Geha, M., et al. 2000: *The MACHO Project: Microlensing Results from 5.7 Years of Large Magellanic Cloud Observations*, ApJ, 542, 281
- An, J. H., Evans, N. W., Hewett, P., Baillon, P., Calchi Novati, S., Carr, B. J., Crézé, M., Giraud-Héraud, Y., Gould, A., Jetzer, P., Kaplan, J., et al. 2004a: *The POINT-AGAPE Survey - I. The variable stars in M31*, MNRAS, 351, 1071
- An, J. H., Evans, N. W., Kerins, E., Baillon, P., Calchi Novati, S., Carr, B. J., Crézé, M., Giraud-Héraud, Y., Gould, A., Hewett, P., Jetzer, P., et al. 2004b: *The Anomaly in the Candidate Microlensing Event PA-99-N2*, ApJ, 601, 845
- Aurière, M., Baillon, P., Bouquet, A., Carr, B. J., Crézé, M., Evans, N. W., Giraud-Héraud, Y., Gould, A., Hewett, P. C., Kaplan, J., Kerins, E., et al. 2001: *A Short-Timescale Candidate Microlensing Event in the POINT-AGAPE Pixel Lensing Survey of M31*, ApJ, 553, L137
- Bertin, E. & Arnouts, S. 1996: *SExtractor: Software for source extraction.*, A&AS, 117, 393
- Calchi Novati, S. 2010: *Pixel lensing. Microlensing towards M31*, General Relativity and Gravitation, 42, 2101



- Calchi Novati, S., Bozza, V., De Paolis, F., Dominik, M., Ingrosso, G., Jetzer, P., Mancini, L., Nucita, A., Scarpetta, G., Sereno, M., Strafella, F., et al. 2009: *Candidate Microlensing Events from M31 Observations with the Loiano Telescope*, ApJ, 695, 442
- Calchi Novati, S., Dall’Ora, M., Gould, A., Bozza, V., Bruni, I., De Paolis, F., Dominik, M., Gualandi, R., Ingrosso, G., Jetzer, P., Mancini, L., et al. 2010: *M31 Pixel Lensing Event OAB-N2: A Study of the Lens Proper Motion*, ApJ, 717, 987
- Calchi Novati, S. & Mancini, L. 2011: *Microlensing towards the LMC: self lensing for OGLE-II and OGLE-III*, ArXiv e-prints
- Calchi Novati, S., Paulin-Henriksson, S., An, J., Baillon, P., Belokurov, V., Carr, B. J., Cr    , M., Evans, N. W., Giraud-H  raud, Y., Gould, A., Hewett, P., et al. 2005: *POINT-AGAPE pixel lensing survey of M 31. Evidence for a MACHO contribution to galactic halos*, A&A, 443, 911
- Crotts, A. P. S. 1992: *M31 - A unique laboratory for gravitational microlensing*, ApJ, 399, L43
- Crotts, A. P. S., Uglesich, R., Gyuk, G., & Tomaney, A. B. 2001: *MEGA, a Wide-Field Survey of Microlensing in M31*, in Astronomical Society of the Pacific Conference Series, Vol. 237, Gravitational Lensing: Recent Progress and Future Go, ed. T. G. Brainerd & C. S. Kochanek, 243–+
- Cseresnjes, P., Crotts, A. P. S., de Jong, J. T. A., Bergier, A., Baltz, E. A., Gyuk, G., Kuijken, K., & Widrow, L. M. 2005: *HST Imaging of MEGA Microlensing Candidates in M31*, ApJ, 633, L105
- Darnley, M. J., Bode, M. F., Kerins, E., Newsam, A. M., An, J., Baillon, P., Belokurov, V., Calchi Novati, S., Carr, B. J., Cr    , M., Evans, N. W., et al. 2006: *Classical novae from the POINT-AGAPE microlensing survey of M31 - II. Rate and statistical characteristics of the nova population*, MNRAS, 369, 257
- Darnley, M. J., Bode, M. F., Kerins, E., Newsam, A. M., An, J., Baillon, P., Novati, S. C., Carr, B. J., Cr    , M., Evans, N. W., Giraud-H  raud, Y., et al. 2004: *Classical novae from the POINT-AGAPE microlensing survey of M31 - I. The nova catalogue*, MNRAS, 353, 571
- de Jong, J. T. A., Widrow, L. M., Cseresnjes, P., Kuijken, K., Crotts, A. P. S., Bergier, A., Baltz, E. A., Gyuk, G., Sackett, P. D., Uglesich, R. R., & Sutherland, W. J. 2006: *MACHOs in M 31? Absence of evidence but not evidence of absence*, A&A, 446, 855

- Fliri, J., Riffeser, A., Seitz, S., & Bender, R. 2006: *The Wendelstein Calar Alto Pixellensing Project (WeCAPP): the M 31 variable star catalogue*, A&A, 445, 423
- Gössl, C. A. & Riffeser, A. 2002: *Image reduction pipeline for the detection of variable sources in highly crowded fields*, A&A, 381, 1095
- Hodapp, K. W., Siegmund, W. A., Kaiser, N., Chambers, K. C., Laux, U., Morgan, J., & Mannery, E. 2004: *Optical design of the Pan-STARRS telescopes*, in Society of Photo-Optical Instrumentation Engineers (SPIE) Conference Series, Vol. 5489, Society of Photo-Optical Instrumentation Engineers (SPIE) Conference Series, ed. J. M. Oschmann Jr., 667–678
- Ingrosso, G., Calchi Novati, S., de Paolis, F., Jetzer, P., Nucita, A. A., Scarpetta, G., & Strafella, F. 2007: *A new analysis of the MEGA M 31 microlensing events*, A&A, 462, 895
- Ingrosso, G., Calchi Novati, S., de Paolis, F., Jetzer, P., Nucita, A. A., & Strafella, F. 2006: *Monte Carlo analysis of MEGA microlensing events towards M 31*, A&A, 445, 375
- Ingrosso, G., Novati, S. C., de Paolis, F., Jetzer, P., Nucita, A. A., & Zakharov, A. F. 2009: *Pixel lensing as a way to detect extrasolar planets in M31*, MNRAS, 399, 219
- Ising, E. 1925: *Beitrag zur Theorie des Ferromagnetismus*, Zeitschrift für Physik, Bd. 31, 253
- Ivezić, Ž., Smith, J. A., Miknaitis, G., Lin, H., Tucker, D. L., Lupton, R., Knapp, G. R., Gunn, J. E., Strauss, M., Holtzman, J., Kent, S., et al. 2007: *A Comparison of SDSS Standard Star Catalog for Stripe 82 with Stetson’s Photometric Standards*, in Astronomical Society of the Pacific Conference Series, Vol. 364, The Future of Photometric, Spectrophotometric and Polarimetric Standardization, ed. C. Sterken, 165
- Kaiser, N., Burgett, W., Chambers, K., Denneau, L., Heasley, J., Jedicke, R., Magnier, E., Morgan, J., Onaka, P., & Tonry, J. 2010: *The Pan-STARRS wide-field optical/NIR imaging survey*, in Society of Photo-Optical Instrumentation Engineers (SPIE) Conference Series, Vol. 7733, Society of Photo-Optical Instrumentation Engineers (SPIE) Conference Series
- Kerins, E., Darnley, M. J., Duke, J. P., Gould, A., Han, C., Jeon, Y.-B., Newsam, A., & Park, B.-G. 2006: *The Angstrom Project: a microlensing survey of the structure and composition of the bulge of the Andromeda galaxy*, MNRAS, 365, 1099



- Riffeser, A., Seitz, S., & Bender, R. 2008: *The M31 Microlensing Event WeCAPP-GL1/POINT-AGAPE-S3: Evidence for a MACHO Component in the Dark Halo of M31?*, ApJ, 684, 1093
- Saglia, R. P., Fabricius, M., Bender, R., Montalto, M., Lee, C.-H., Riffeser, A., Seitz, S., Morganti, L., Gerhard, O., & Hopp, U. 2010: *The old and heavy bulge of M 31 . I. Kinematics and stellar populations*, A&A, 509, A61+
- Sahu, K. C. 1994: *Stars Within the Large Magellanic Cloud as Potential Lenses for Observed Microlensing Events*, Nature, 370, 275
- Stetson, P. B. 1987: *DAOPHOT - A computer program for crowded-field stellar photometry*, PASP, 99, 191
- Tang, A., Jackson, D., Hobbs, J., Chen, W., Smith, J. L., Patel, H., Prieto, A., Petrusca, D., Grivich, M. I., Sher, A., Hottowy, P., et al. 2008: *A Maximum Entropy Model Applied to Spatial and Temporal Correlations from Cortical Networks In Vitro*, The Journal of Neuroscience, 28, 505
- Tempel, E., Tuvikene, T., Tamm, A., & Tenjes, P. 2011: *SDSS surface photometry of M 31 with absorption corrections*, A&A, 526, A155+
- Tisserand, P., Le Guillou, L., Afonso, C., Albert, J. N., Andersen, J., Ansari, R., Aubourg, É., Bareyre, P., Beaulieu, J. P., Charlot, X., Coutures, C., et al. 2007: *Limits on the Macho content of the Galactic Halo from the EROS-2 Survey of the Magellanic Clouds*, A&A, 469, 387
- Tonry, J. & Onaka, P. 2009: *The Pan-STARRS Gigapixel Camera*, in Advanced Maui Optical and Space Surveillance Technologies Conference,
- Tonry, J. L., Stubbs, C. W., Lykke, K., Doherty, P., Burgett, W. S., Chambers, K. C., Flewelling, H., Grav, T., Heasley, J. N., Hodapp, K. W., Jedicke, R., et al. 2012: *The Pan-STARRS 1 Photometric System*, in prep.
- Valentijn, E. A., McFarland, J. P., Snigula, J., Begeman, K. G., Boxhoorn, D. R., Rengelink, R., Helmich, E., Heraudeau, P., Kleijn, G. V., Vermeij, R., Vriend, W.-J., et al. 2007: *Astro-WISE: Chaining to the Universe*, in Astronomical Society of the Pacific Conference Series, Vol. 376, Astronomical Data Analysis Software and Systems XVI, ed. R. A. Shaw, F. Hill, & D. J. Bell, 491–+
- Wyrzykowski, L., Kozłowski, S., Skowron, J., Belokurov, V., Smith, M. C., Udalski, A., Szymański, M. K., Kubiak, M., Pietrzyński, G., Soszyński, I., & Szewczyk, O. 2010:

*The OGLE view of microlensing towards the Magellanic Clouds - II. OGLE-II Small Magellanic Cloud data*, MNRAS, 407, 189

Wyrzykowski, L., Kozłowski, S., Skowron, J., Belokurov, V., Smith, M. C., Udalski, A., Szymański, M. K., Kubiak, M., Pietrzyński, G., Soszyński, I., Szewczyk, O., et al. 2009: *The OGLE view of microlensing towards the Magellanic Clouds - I. A trickle of events in the OGLE-II LMC data*, MNRAS, 397, 1228

Wyrzykowski, L., Kozłowski, S., Skowron, J., Udalski, A., Szymański, M. K., Kubiak, M., Pietrzyński, G., Soszyński, I., Szewczyk, O., Ulaczyk, K., & Poleski, R. 2011a: *The OGLE view of microlensing towards the Magellanic Clouds - III. Ruling out subsolar MACHOs with the OGLE-III LMC data*, MNRAS, 413, 493

Wyrzykowski, L., Skowron, J., Kozłowski, S., Udalski, A., Szymanski, M. K., Kubiak, M., Pietrzyński, G., Soszyński, I., Szewczyk, O., Ulaczyk, K., Poleski, R., et al. 2011b: *The OGLE View of Microlensing towards the Magellanic Clouds. IV. OGLE-III SMC Data and Final Conclusions on MACHOs*, ArXiv e-prints